

Fall 2007

Simulation and Fabrication of Three Novel Micromechanical Sensors

Yanqing Lu
Louisiana Tech University

Follow this and additional works at: <https://digitalcommons.latech.edu/dissertations>



Part of the [Mechanical Engineering Commons](#)

Recommended Citation

Lu, Yanqing, "" (2007). *Dissertation*. 505.
<https://digitalcommons.latech.edu/dissertations/505>

This Dissertation is brought to you for free and open access by the Graduate School at Louisiana Tech Digital Commons. It has been accepted for inclusion in Doctoral Dissertations by an authorized administrator of Louisiana Tech Digital Commons. For more information, please contact digitalcommons@latech.edu.

**SIMULATION AND FABRICATION OF
THREE NOVEL MICROMECHANICAL
SENSORS**

by

Yanqing Lu, M. S.

A Dissertation Presented in Partial Fulfillment
of the Requirement for the Degree
Doctor of Philosophy

COLLEGE OF ENGINEERING AND SCIENCE
LOUISIANA TECH UNIVERSITY

November, 2007

UMI Number: 3285244

INFORMATION TO USERS

The quality of this reproduction is dependent upon the quality of the copy submitted. Broken or indistinct print, colored or poor quality illustrations and photographs, print bleed-through, substandard margins, and improper alignment can adversely affect reproduction.

In the unlikely event that the author did not send a complete manuscript and there are missing pages, these will be noted. Also, if unauthorized copyright material had to be removed, a note will indicate the deletion.

UMI[®]

UMI Microform 3285244

Copyright 2007 by ProQuest Information and Learning Company.

All rights reserved. This microform edition is protected against unauthorized copying under Title 17, United States Code.

ProQuest Information and Learning Company
300 North Zeeb Road
P.O. Box 1346
Ann Arbor, MI 48106-1346

LOUISIANA TECH UNIVERSITY

THE GRADUATE SCHOOL

10/16/2007

Date

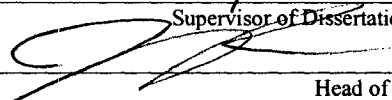
We hereby recommend that the dissertation prepared under our supervision
by Yanqing Lu

entitled Simulation and Fabrication of Three Novel Micromechanical Sensors

be accepted in partial fulfillment of the requirements for the Degree of
Ph.D. in Engineering



Supervisor of Dissertation Research



Head of Department

Department

Recommendation concurred in:

Yeevi Luov

[Signature]

Sabbetha G. [Signature]

[Signature]

Advisory Committee

Approved:

[Signature]

Director of Graduate Studies

Approved:

[Signature]

Dean of the Graduate School

[Signature]

Dean of the College

GS Form 13a
(6/07)

ABSTRACT

This work focuses on the simulation, fabrication and characterization of novel microdevices for chemical and biological sensors for improved sensitivity, enhanced performance and applicability. Specifically, microbridge and microcoil sensors have been fabricated via advanced microfabrication technologies. Due to the potential application in chemical and biological sensing, the growth of gold and platinum nanowires during an electrolysis process have also been investigated.

A microbridge can be considered as the head-to-head fusion of two cantilevers and the middle of the bridge would deform in a way similar to a microcantilever. The microbridge sensing device is more stable than the microcantilever, especially in turbulent or vibrational conditions, since both ends are fixed. The trade-off is the low $\Delta R/R$ change (sensitivity) of the microbridge compared to that of the microcantilever. Simulation of the microbridge has been conducted via Finite Element Analysis (FEA). The width, thickness and doping level of the piezoresistor play an important part in the sensitivity of the microbridge. Based on the simulation results and following standard microfabrication technology, microbridges have been fabricated. The detection of Hg^{2+} based on the microbridge platform was investigated for sensor validation.

The microcoil hygrometer can be used as a universal tool for the detection of chemical species by depositing a chemical specific coating on one side of the coil. The coil movement can be readily observed by the human eye and it advances as a

cost-effective and power-free device. A micro- or nano-scale sized coil provides an outstanding sensor platform with improved dynamic response, greatly reduced size, and the integration of micromechanical components with on-chip electronic circuitry. Following standard microfabrication techniques, an $\text{SiO}_2/\text{Si}/\text{SU-8}$ microcoil has been fabricated. After surface modification by treating the coil with aminopropyltriethoxysilane (APS), the microcoil was exposed to acetic acid vapor in air for characterization. This microcoil device has a potential to be used as a novel microsensor for the detection of chemical and biological species both in air and in solutions.

A self-assembled approach to grow gold and platinum nanowires across the gap of two electrodes on a surface using an electrolysis process has been investigated. In this process, the anode electrode is oxidized to form nanowires on the cathode. The DC offset, AC signal frequency and the space between the two electrodes all play important roles in the growth of the nanowires.

APPROVAL FOR SCHOLARLY DISSEMINATION

The author grants to the Prescott Memorial Library of Louisiana Tech University the right to reproduce, by appropriate methods, upon request, any or all portions of this Dissertation. It is understood that "proper request" consists of the agreement, on the part of the requesting party, that said reproduction is for his personal use and that subsequent reproduction will not occur without written approval of the author of this Dissertation. Further, any portions of the Dissertation used in books, papers, and other works must be appropriately referenced to this Dissertation.

Finally, the author of this Dissertation reserves the right to publish freely, in the literature, at any time, any or all portions of this Dissertation.

Author Yanqing Lu *Yanqing Lu*

Date 10/16/2007

TABLE OF CONTENTS

ABSTRACT.....	iii
TABLE OF CONTENTS.....	vi
LIST OF TABLES.....	ix
LIST OF FIGURES.....	x
ACKNOWLEDGMENTS.....	xiv
CHAPTER ONE INTRODUCTION.....	1
1.1 Chemical and Biological Sensors.....	1
1.2 Microfabrication Technologies.....	7
1.2.1 Lithography.....	7
1.2.2 Spin-coating.....	10
1.2.3 Etching.....	11
1.2.4 Metallization.....	18
1.2.5 Oxidation.....	21
1.2.6 Thin Film Deposition.....	22
1.3 Research Objectives.....	24
1.4 Dissertation Outline.....	25
CHAPTER TWO EXPERIMENTAL MATERIALS AND EQUIPMENTS.....	26
2.1 Experimental Materials.....	26
2.1.1 Si.....	26
2.1.2 SU-8.....	27

2.1.3 PDMS.....	30
2.1.4 PR1813.....	32
2.2 Experimental Equipments.....	33
2.2.1 SEM	33
2.2.2 AFM	34
2.2.3 Surface Profilometer	36
CHAPTER THREE SIMULATION AND FABRICATION OF MICROBRIDGES.....	37
3.1 Introduction.....	37
3.2 Finite Element Model	40
3.3 Results and Discussion	46
3.3.1 Effect of thickness of piezoresistor on the microbridge arcuation and fractional change in resistance of the microbridge (R/R).....	46
3.3.2 Effect of doping concentrations of the piezoresistor on the $\Delta R/R$ changes.....	51
3.4 Fabrication of SiO ₂ microbridge with Si piezoresistors	53
3.5 Conclusion	58
CHAPTER FOUR MICROCOILS FOR CHEM/BIO SENSING.....	60
4.1 Introduction.....	60
4.2 Power-free Coil Sensors	61
4.3 Microcoil Sensors	63
4.4 Fabrication Process	64
4.5 Results and Discussions.....	68
4.6 Sensing Behavior of the Microcoils.....	71
4.7 Conclusions.....	75

CHAPTER FIVE FABRICATION AND CHARACTERIZATION OF GOLD AND PLATINUM NANOWIRES	77
5.1 Introduction.....	77
5.2 Experiments	78
5.3 Results and Discussions.....	80
5.4 Conclusions.....	83
CHAPTER SIX CONCLUSIONS AND FUTURE WORK	84
6. 1 Conclusions.....	84
6. 2 Future Work.....	86
REFERECES	87

LIST OF TABLES

Table 1 Common materials and their plasma etchants in dry etching [22]	17
Table 2 Material properties of Si with surface stress at [110] direction used in the simulation.....	45
Table 3 Material properties of SiO ₂ used in the simulation.....	45

LIST OF FIGURES

Figure 1.1 Different types of microcantilevers [4].	2
Figure 1.2 SEM image of SiO ₂ microcantilevers [6].	3
Figure 1.3 Microcantilever bending due to the surface stress induced by analyte adsorption [10].	4
Figure 1.4 Schematic of an optical detection system for detecting microcantilever deflection [4].	4
Figure 1.5 Application of microcantilever-based sensors [4].	6
Figure 1.6 The process of photolithography.	8
Figure 1.7 Four stages of the spin-coating process [19].	11
Figure 1.8 Isotropic and anisotropic etching profiles [20].	12
Figure 1.9 Anisotropic etching of Si.	13
Figure 1.10 Alcatel 601E ICP equipment.	14
Figure 1.11 Schematics of the principle of plasma etching [20].	15
Figure 1.12 Sketch of an ICP coil chamber. The axial magnetic field induces an azimuthal electric field, which accelerates the charged particles [21].	16
Figure 1.13 Schematic process of ICP etching system [23].	18
Figure 1.14 Lift-off procedure for patterning metal.	20
Figure 1.15 Improved lift-off with two-layers of photoresist and the bottom layer undercut.	21
Figure 1.16 Typical e-beam evaporation system [24].	23
Figure 1.17 The principle of a sputtering system [25].	24
Figure 2.1 Diamond unit cell of Si [25].	27

Figure 2.2 Standard process procedures for SU-8 [27].....	28
Figure 2.3 Spin-coating recipe for SU-8.....	29
Figure 2.4 Standard PDMS process procedures.	31
Figure 2.5 Spin-coating recipe of PR 1813.....	33
Figure 2.6 Amray 1830 SEM.....	34
Figure 2.7 (a) Operating principle of the AFM and (b) the tip of the AFM [28].	35
Figure 2.8 KLA Tencor profilometer.....	36
Figure 3.1 (a) Schematic of the bending of a microbridge due to analyte adsorption; (b) the microbridge under the effect of net surface stress $\Delta\sigma$, due to physical absorption on the bridge surface and (c) the resultant arcuation of the bridge in z direction.	38
Figure 3.2 Flowchart of CoventorWare simulation process.	43
Figure 3.3 Schematic model of a Si covered SiO ₂ microbridge.	44
Figure 3.4 The (a) $\Delta R/R$ and (b) arcuation of SiO ₂ microbridge vs. the thickness of Si piezoresistor on the microbridge, when a surface stress of 2 N/m was applied on the surface of SiO ₂ microbridge. c) $\Delta R/R$ vs. the arcuation of the SiO ₂ microbridge. The dimensions of the SiO ₂ microbridges were 400 μm in length (L_c), 50 μm in width (W_c), and 1 μm in thickness. The Si piezoresistors were 400 μm in length (L_p) and width varying from 2 μm to 10 μm . The doping concentration is $1 \times 10^{17} \text{ cm}^{-3}$	47
Figure 3.5 Effect of (a) voltage variation, (b) temperature variation on the $\Delta R/R$ change of microbridges with different thicknesses. The SiO ₂ microbridges were 400 μm in length, 50 μm in width, and 1 μm in thickness. The piezoresistors were 400 μm in length, 2 μm in width, with the thickness varying from 0.2 μm to 2 μm . The doping concentration is $1 \times 10^{17} \text{ cm}^{-3}$	49
Figure 3.6 S/N ratio of microbridges with the thickness of the piezoresistor varying from 0.2 μm to 2 μm . The SiO ₂ microbridges were 400 μm in length, 50 μm in width, and 1 μm in thickness. The piezoresistors were 400 μm in length and 2 μm in width. The doping concentration is $1 \times 10^{17} \text{ cm}^{-3}$	50
Figure 3.7 The $\Delta R/R$ vs. doping concentration when a 2 N/m surface stress is applied on the surface of an SiO ₂ microbridge. The boron doping concentrations were from 1×10^{16} to $5 \times 10^{19} \text{ cm}^{-3}$. The dimensions of	

the SiO ₂ microbridge were 400 μm in length, 50 μm in width, and 1 μm in thickness. The piezoresistors were 400 μm in length, 2 μm in width, and 2 μm in thickness.	53
Figure 3.8 Fabrication process for SiO ₂ supported piezoresistive microbridges.	56
Figure 3.9 SEM picture of piezoresistive Si on an SiO ₂ microbridge. The dimensions of the SiO ₂ microbridge were 400 μm in length, 50 μm in width, and 1 μm in thickness. The piezoresistor was 400 μm in length, 10 μm in width, and 2 μm in thickness.	57
Figure 3.10 The resistance change of a piezoresistive Si on SiO ₂ microbridge upon exposure to a 10 ⁻⁶ M of Hg ²⁺ . The dimensions of the SiO ₂ microbridge were 400 μm in length, 50 μm in width, and 1 μm in thickness. The piezoresistor was 400 μm in length, 10 μm in width, and 2 μm in thickness.	58
Figure 4.1 The SEM picture of a SiO ₂ /Si/SU-8 trilayered microcoil and array. In the extended form, the dimensions of the microcoil were 9.8 mm in length, 50 μm in width, and 28 μm in thickness. The coil size was 500 μm × 600 μm. The thickness of the Si and SU-8 layer were 8 and 20 μm, respectively. For fabrication simplicity, the coil was made in a structure that the two ends of the coil were attached to two pads outside of the coil. To match with this structure, the specially designed SU-8 layer was kept on the outside surfaces of the coil in order to achieve a uniform contraction or expansion of the coil, i.e. the SU-8 layer from the bottom pad to the center was not connected with the SU-8 from the top pad to the center.	64
Figure 4.2 Fabrication process for the microcoils.	68
Figure 4.3 Microcoils fabricated using an ICP recipe with 1800W power, 300 sccm SF ₆ , 50 sccm C ₄ F ₈ , 30W bias power and 18% pressure.	69
Figure 4.4 Microcoil developed after (a) 120 seconds and (b) 50 seconds exposure to the UV light.	71
Figure 4.5 The coil movement when the inside surface is expanded (left) or contracted (right).	72
Figure 4.6 Monolayer reaction of APS on Si surface [92].	73
Figure 4.7 The resistance change of (a) an aminopropyltriethoxy-silane modified Si/SU-8 bilayered micro-spiral spring and (b) a piezoresistive microcantilever before and after exposure to 2.1% acetic acid in air. In the extended form, the dimensions of the microcoil were 7.7 mm in length, 50 μm in width, and 28 μm in thickness. The dimensions	

of the SiO ₂ cantilever were 250 μm in length, 100 μm in width, and 1 μm in thickness. The Si piezoresistors on the SiO ₂ cantilever was 100 μm in length, 20 μm in width, and 2 μm in thickness.	74
Figure 5.1 A schematic diagram of the gold electrodes. The electrodes were made on a Si wafer covered by 300-nm-thick SiO ₂	78
Figure 5.2 (a) Optical and (b) SEM images of the gold nanowires grown from an electrolysis process under an AC signal of 7 Vrms and 1 MHz with an DC offset of 10 V. The original gap between the two gold electrodes was 5 μm.....	79
Figure 5.3 EDS analysis of the components of the gold nanowires and the adjacent SiO ₂ surface.	80
Figure 5.4 SEM images of the platinum nanowires grown from the electrolysis process under an AC signal of 9 Vrms and 10 Hz with an DC offset of 13 V.	82
Figure 5.5 EDS component analysis of the Pt nanowires.	83

ACKNOWLEDGMENTS

I would like to thank my advisor, Dr. Haifeng Ji, for his invaluable advice, continuous guidance, encouragement and support. Special acknowledgments are extended to Mr. Ji Fang, Dr. Sidney Sit, Dr. Yuri Lvov and Dr. Tabbetha Dobbins for their advice and serving as advisory committee members for this dissertation.

I would also like to thank the staff at Institute for Micromanufacturing (IfM), especially Dr. Karen Xu, Donald Tatum, Dr. Alfred Gunasekaran and John McDonald for their help and support on the microfabrication processes as well as metrology instruments. Much gratitude is extended to all my fellow group members for their invaluable discussion, support, and cooperation.

Finally, I dedicate this dissertation to my family whose love and encouragement accompanied me throughout this research.

CHAPTER ONE

INTRODUCTION

1.1 Chemical and Biological Sensors

The fabrication of the chemical and biological sensors utilizing silicon (Si) microfabrication technologies has been the focus of intensive research for many years mainly because advances in technology have made mass-production and low-cost devices possible [1]. Chemical and biological sensors span a wide range of sensor devices and measurement instrument functionalities. Their applications include, but are not limited to, the detection of:

- 1) the gross characteristics of the overall chemical or biological environment;
- 2) the concentration or even just the presence of particular chemical or biological species;
- 3) the elemental constituents of a mixture;
- 4) the molecular structure of a pure compound or a mixture of compounds;
- 5) the structure of a bulk material and identify its atomic constituents and three-dimensional molecular arrangements [2].

Among these applications of chemical and biological sensors, one of the most important applications is to detect the concentration (or just the presence) of particular chemical or biological species, or in other words, chemical or biological sensing.

Since the introduction of the first microcantilever sensor in 1994 by Thomas Thundat at the Oak Ridge National Laboratory (ORNL) for humidity detection [3], many efforts have been undertaken to develop chemical and biological sensors based on microcantilevers. The advances in microfabrication techniques has now made it possible to mass-produce miniaturized sensors with high sensitivity.

Microcantilevers are one of the major devices in Micro-Electro-Mechanical Systems (MEMS). They have long, ultra thin flexible beams with tips at the front end. Figure 1.1 shows different types of microcantilevers [4]. The typical dimensions of the microcantilevers are $0.2\ \mu\text{m}$ to $1\ \mu\text{m}$ in thickness, $20\ \mu\text{m}$ to $100\ \mu\text{m}$ in width and $100\ \mu\text{m}$ to $500\ \mu\text{m}$ in length. Si and silicon nitride (Si_3N_4) are the most widely used materials for fabricating microcantilevers [5]. In our group, silicon dioxide (SiO_2) microcantilevers have also been successfully fabricated by Y. Tang as shown in Figure 1.2 [6].

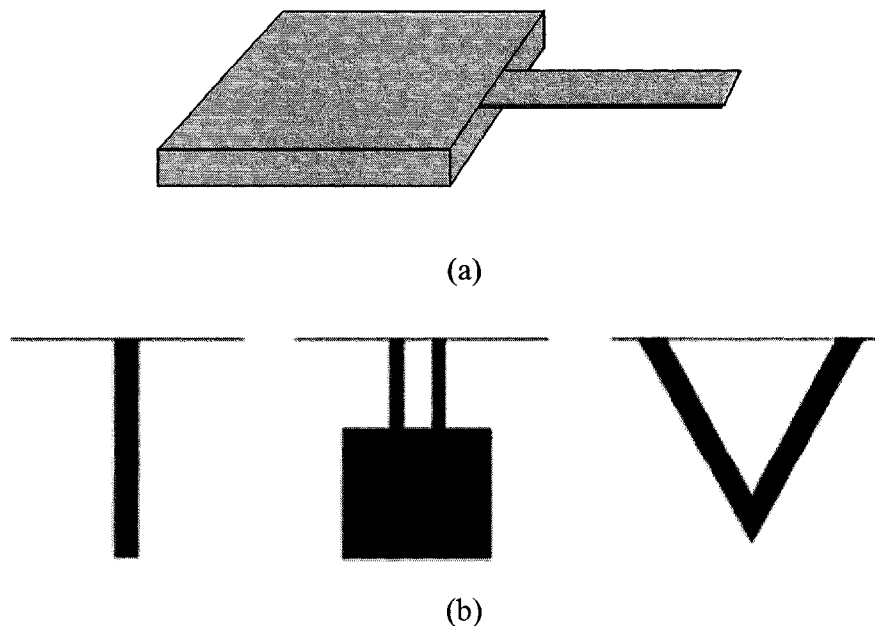


Figure 1.1 Different types of microcantilevers [4].

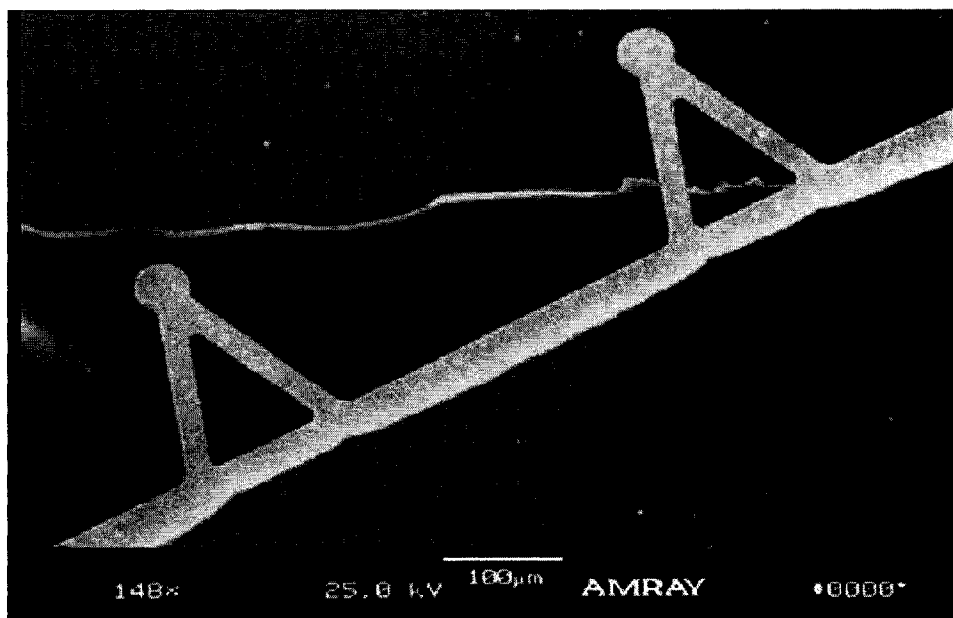


Figure 1.2 SEM image of SiO₂ microcantilevers [6].

The principle of a microcantilever is that its amplitude, frequency, deflection or Q-factor changes due to adsorption of chemicals on the cantilever surface or changes in the environment [3]. By monitoring the changes in the responses, humidity, viscosity, pressure, density, temperature, flow rate, pH and the presence of radiation in the surrounding environment could be accurately detected [7] - [9]. The microcantilever in Figure 1.3 [10] shows bending of a microcantilever due to analyte adsorption induced surface stress. The magnitude of the bending is proportional to the concentration of the analyte. Figure 1.4 [4] schematically illustrates the optical approach to detect the deflection of a microcantilever. A laser beam from a laser diode is shined on the microcantilever tip (usually coated with a thin layer of gold) and is reflected off the microcantilever to be received by a position sensitive photodetector. The photodetector converts the optical signal into an electrical signal and sends it to a computer. By

comparing the signal with a reference signal, the concentration of the analyte could be accurately determined.

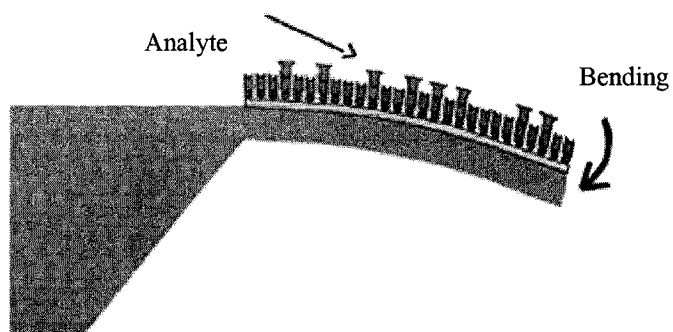


Figure 1.3 Microcantilever bending due to the surface stress induced by analyte adsorption [10].

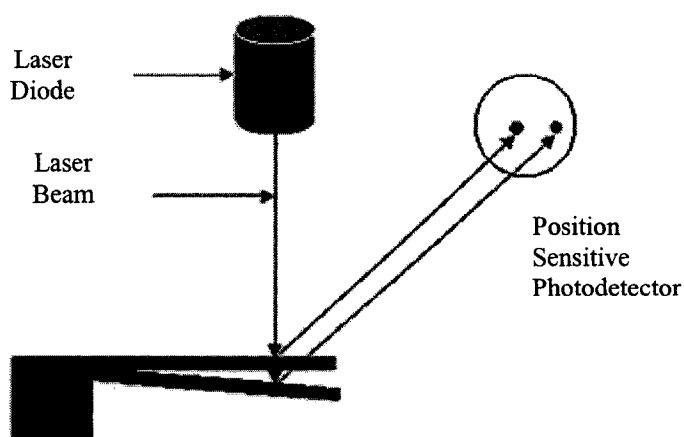


Figure 1.4 Schematic of an optical detection system for detecting microcantilever deflection [4].

In general, the microcantilever technology has several advantages [4]:

- First, sensitivity. The ability to measure cantilever motion with sub-nanometer precision allows for ppt level detection of chemicals.
- Second, low analyte requirement. The entire sensor could fit in an area with dimensions less than a few millimeters on a side. The corresponding

analyte requirement is very low due to the small size of the microcantilevers.

- Third, low cost. Hundreds of microcantilevers could be fabricated on a single wafer. Electronics for operation and control are relatively simple and inexpensive.
- Fourth, non-hazardous procedures. It is safe to operate a microcantilever, and there is no waste generated from the operation when compared with traditional chemical assays.

Due to the advantages listed above, microcantilevers have been extensively explored in their application as chemical and biological sensors, as shown in Figure 1.5 [4]. Microcantilevers can be used both in air and in solutions to detect chemical agents. They have been investigated to detect chemical traces of HF, Cs⁺, CrO₄, Ca²⁺ and Hg²⁺ in solutions [11] - [15]. In their application as biological sensors, microcantilevers have been used to detect DNA, antigen and biomarkers [16] - [18].

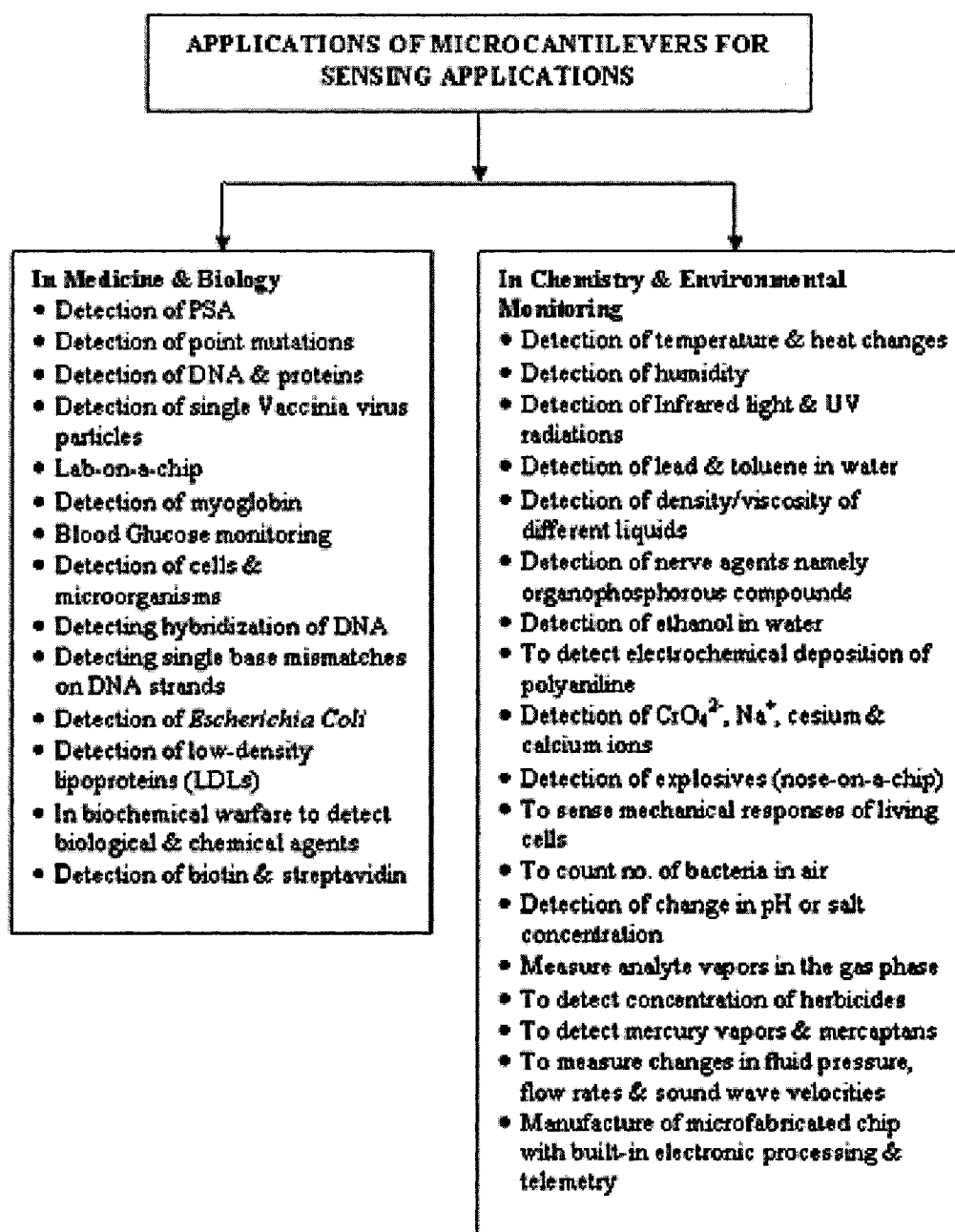


Figure 1.5 Application of microcantilever-based sensors [4].

In spite of all the advantages, there still remain stability problems associated with the microcantilevers when they are applied on a mobile vehicle or moving object, and there is a need to improve the sensitivity of the microcantilevers toward enhancing their performance and applicability.

1.2 Microfabrication Technologies

The design and fabrication of the micro- chemical and biological sensors are based on microfabrication technologies, which have been used for many years in the MEMS and microelectronics fields. Microfabrication technologies originate from the microelectronic industry, and the devices are usually made from Si, although glass, plastics, polymers and many other materials are also in use. Si planar technology is currently the principle processing method in the fabrication of most Si integrated circuits and devices, the history of which may be dated back to 1959 when this new process was developed at Fairchild Semiconductor.

Si planar technology is actually a collection of technologies which are utilized in fabricating microdevices. Basic Si planar processing steps include epitaxial growth, oxidation, lithography, etching, diffusion, deposition, metallization, interconnections, circuit testing, bonding and encapsulation.

1.2.1 Lithography

The technology to transfer a master pattern onto the surface of a material, such as a Si wafer, is called lithography. Lithography is usually the first step in microfabrication. Among the various lithography technologies including e-beam and x-ray lithography, photolithography has been the most widely used due to its simplicity and low cost. In the IC industry, pattern transfer from masks onto thin films is accomplished almost exclusively via photolithography. The basic idea of photolithography is to use a mask to selectively expose part of the photoresist-coated wafer to UV light while protecting the rest of the wafer from exposure. After exposure, part of the photoresist on the wafer becomes more soluble in the developing solution than the other areas due to chemical

changes in the exposed region. If the exposed area is more soluble than the unexposed area and is thus removed by the developer, the photoresist is called positive tone. On the other hand, if the unexposed area is more soluble and removed by the developer, the photoresist is negative tone. Figure 1.6 shows the process of photolithography and the difference between positive photoresist and negative photoresist.

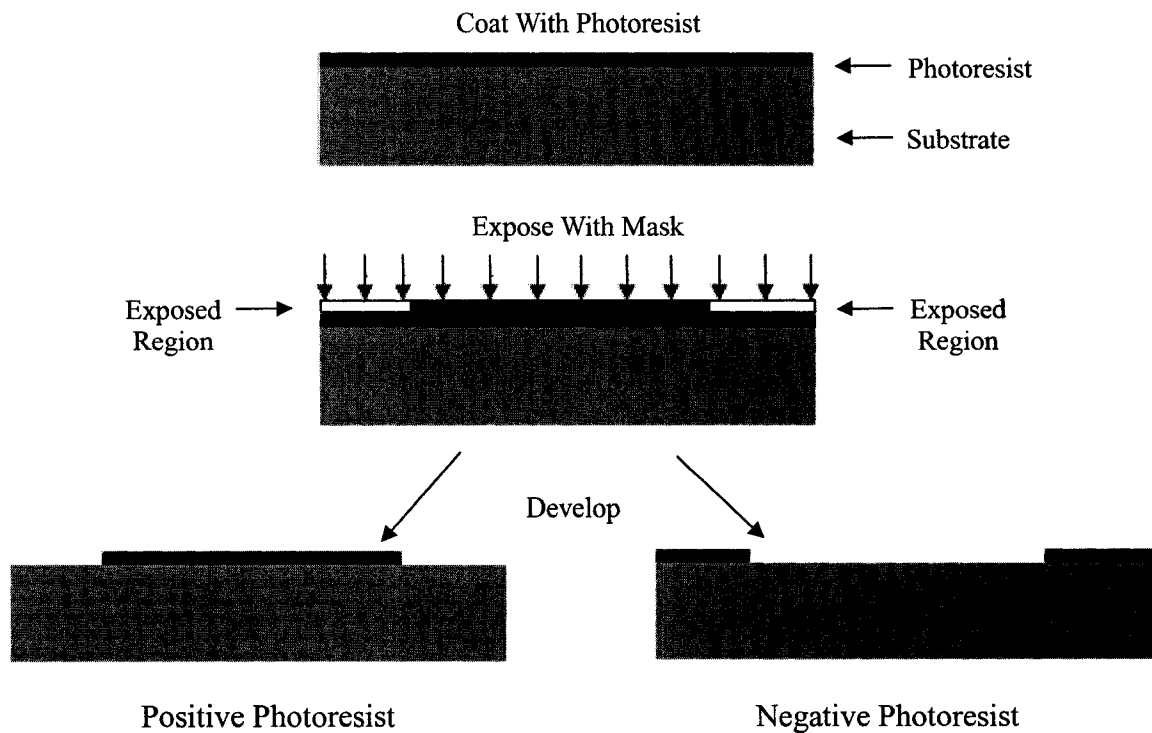


Figure 1.6 The process of photolithography.

A detailed process for photolithography is shown below.

- First, surface clean. The feature size of the microfabricated device is usually very small, therefore any contaminants on the wafer would be a potential problem to the success of the fabrication. Organic contaminants would also cause coating and adhesion problems if the wafer is not completely cleaned before use.

- Second, hard bake. Before it is used, the wafer is hard baked in the oven at 500 °C for 5 minutes to reduce the moisture level on the wafer surface for better coating uniformity and improved adhesion of the photoresist.
- Third, coating the wafer with photoresist. The photoresist is spin-coated onto the surface of the prepared wafer via a spinner at a selected speed to obtain a uniform thickness. Occasionally, when moisture in the air is high, photoresist promoter is first spin-coated on the wafer prior to coating with photoresist to enhance the adhesion between the photoresist and the wafer.
- Fourth, soft bake. The wafer is baked in an oven to evaporate part of the solvents, improve the adhesion and anneal away any stress in the resist that was introduced during the spin-coating process.
- Fifth, wafer alignment and exposure. The wafer is loaded into a mask aligner and exposed to UV light. The mask pattern is transferred to the resist coated wafer through this step.
- Sixth, development. The wafer is immersed into the photoresist developer to remove unwanted areas and keep only the desired pattern on the wafer. The wafer needs to be inspected frequently during this step since either underdevelopment or overdevelopment would seriously affect the quality of the fabricated devices.

Once the above steps are completed, the wafer is ready for subsequent processes such as etching, deposition, lift-off, etc. The photoresist must be removed from the substrate after it is no longer needed. This usually requires a liquid photoresist stripper to chemically dissolve the photoresist. Alternatively, photoresist may be removed via a dry

etching process called ashing. In ashing, a plasma containing oxygen oxidizes and removes the photoresist from the wafer.

1.2.2 Spin-coating

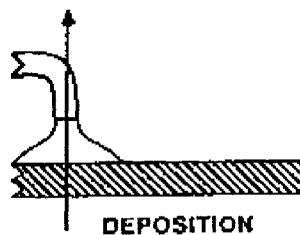
Spin coating is the best way to apply a uniform thin film, such as photoresist, to flat substrates. In spin coating, a spinner rotates at high speed to spin off any extra photoresist on the wafer until the desired thickness of the photoresist is reached. The advantage of spin coating is that the process is simple, safe, and inexpensive. In practice, spin coating can be divided into four distinct stages, as shown in Figure 1.7 [19].

Firstly, the photoresist is transferred to the center area of the wafer by a pipette. Usually, more photoresist than required is used since any extra photoresist would be expelled from the wafer by centrifugal force.

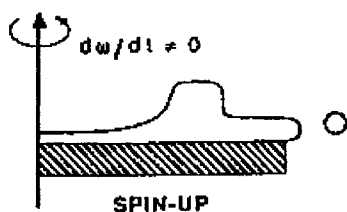
Secondly, the spinner is accelerated to its preprogrammed speed, and rotational forces spread the photoresist until it covers the wafer. Any excess resist is expelled from the wafer.

Thirdly, the spinner rotates at a constant speed and, as excess photoresist continues to be expelled from the wafer, the photoresist continues to get thinner. Viscous fluid force dominates this stage.

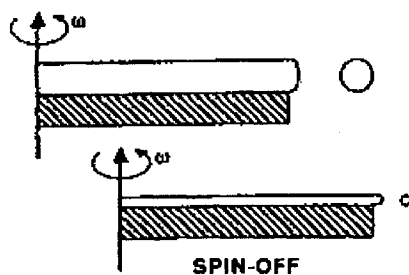
In the last stage, solvent evaporation dominates the photoresist thinning process. Eventually, an extremely thin and uniform film of photoresist is obtained.



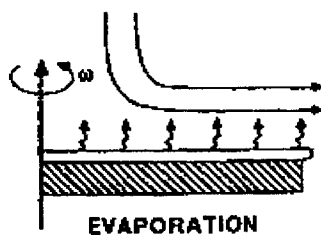
(a) First stage of spin-coating



(b) Second stage of spin-coating



(c) Third stage of spin-coating



(d) Fourth stage of spin-coating

Figure 1.7 Four stages of the spin-coating process [19].

1.2.3 Etching

Etching is the process in microfabrication used for removing unwanted materials either by a physical or a chemical method. Using the protective mask layer generated by the lithography process, materials, such as Si or SiO₂, are removed selectively from the

substrate. For some applications, the protective mask is photoresist while for other applications more durable masks, such as SiO_2 or Si_3N_4 , may be needed and is dependent on the materials to be etched and the duration of the etching process.

Generally speaking, etching falls into two categories, isotropic etching and anisotropic etching. Figure 1.8 shows the difference between the profiles generated via isotropic and anisotropic etching of single crystal materials [20].

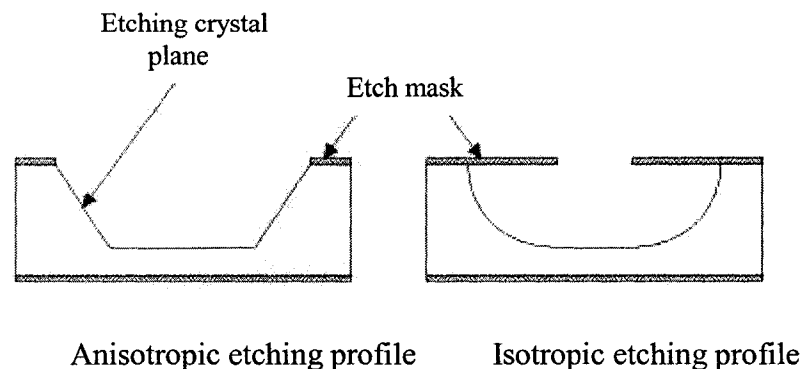


Figure 1.8 Isotropic and anisotropic etching profiles [20].

Etching may be divided into wet etching and dry etching according to the etchants used. In wet etching, the wafer is usually immersed into a bath of etchant. Buffered hydrofluoric acid (HF) is commonly used to etch SiO_2 on a Si substrate and potassium hydroxide (KOH) is commonly used to etch Si.

Figure 1.9 shows the structures of a Si wafer with (100) orientation formed after KOH etching. Since there are far more atoms in crystal Si arranged along the $\langle 111 \rangle$ plane than along other planes, a sloping sidewall of 54.7° is formed during the etching process. If the opening of the mask is narrow, V shaped groves would be formed as shown in Figure 1.9.

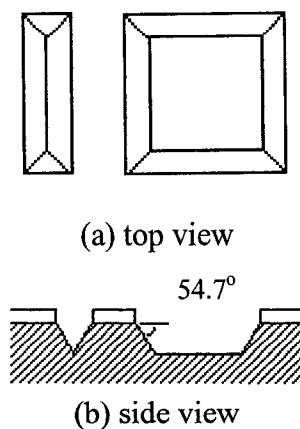


Figure 1.9 Anisotropic etching of Si.

Although wet etching has been extensively used in microfabrication, it has many problems. The capillary action of wet etching would cause penetration of the etchant under the mask and result in ragged edges. Also, large amounts of waste products are produced during the wet etching process, thus being environmentally undesirable.

As an alternative to wet etching, dry etching usually employs a gas to either physically bombard or chemically react with the target to remove the unwanted part of the patterned wafer. Dry etching is highly directional. Anisotropic etching can be obtained by adjusting dry etching parameters such as flow rate, pressure and power. Another advantage of dry etching compared with wet etching is that it is more environmentally desirable since it doesn't produce as much waste products.

In IfM, dry etching is usually done via Inductively Coupled Plasma (ICP, Alcatel 601E) as shown in Figure 1.10 and Deep Reactive Ion Etching (DRIE). ICP etching was used extensively to fabricate the microbridge and microcoil structures for this work. The following section in this chapter describes dry etching in detail, since it is one of the most important steps used in fabricating the micro devices in this dissertation.



Figure 1.10 Alcatel 601E ICP equipment.

Plasma, by its nature, is a highly ionized gas. It is composed of ionized particles with positive or negative charges but is neutral as a whole. This property makes it chemically highly reactive and very useful in microfabrication for etching materials. In dry etching, plasma is usually produced from a gas by applying electromagnetic excitation. Figure 1.11 is a schematic picture illustrating the principle of plasma etching.

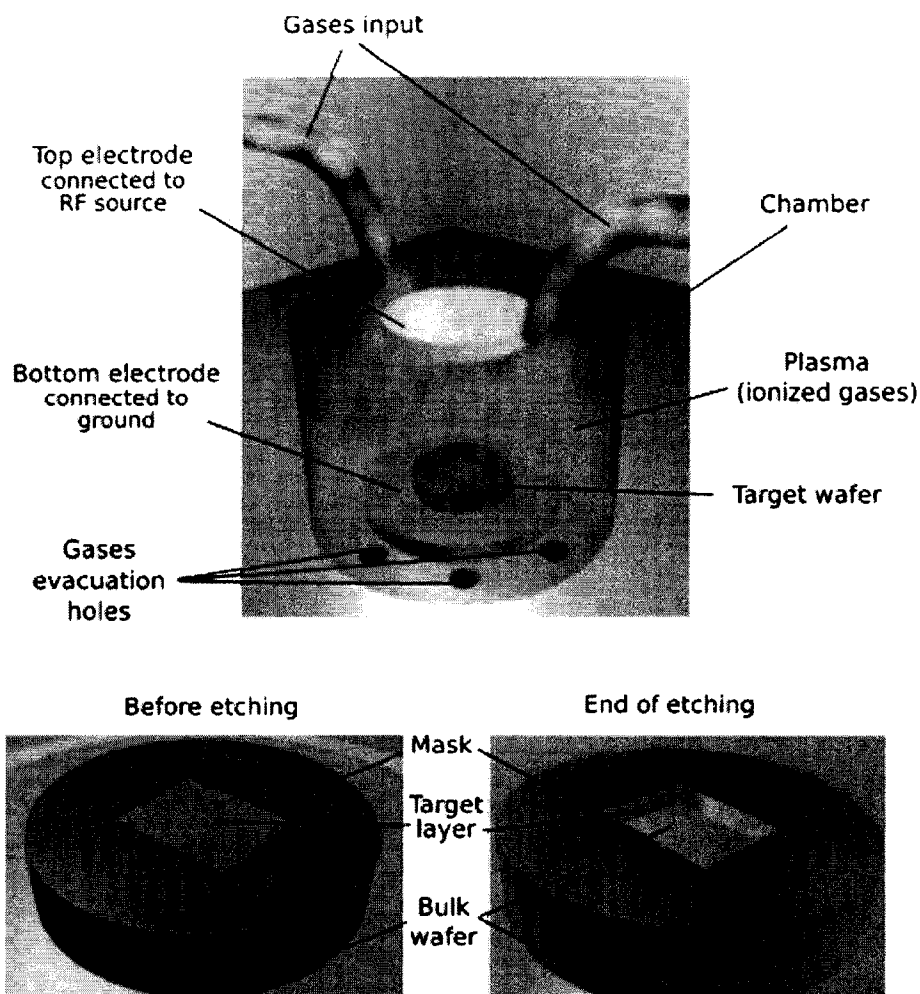


Figure 1.11 Schematics of the principle of plasma etching [20].

As can be seen from Figure 1.11, the top electrode of the plasma etcher is connected to the RF source with a frequency of 13.56 MHz, which is internationally assigned for plasma etching equipment usage. By the excitation of the RF power, the gases in the chamber of the system are ionized and bombard the target wafer positioned on the bottom electrode. At the bottom of the system, the gas evacuation holes remove the gaseous wastes from the chamber, thus sustaining the progress of the etching. In DRIE, a variation of plasma etching, plasma is generated by a magnetic field, and then

densified by a second magnetic field generator. The objective is to reach a high ionization rate in the gases to enhance the etching effect [21].

In an Inductively Coupled Plasma system (ICP) as shown in Figure 1.12 [21], a coil surrounding the reaction chamber generates a magnetic and azimuthal electrical field. This electrical field accelerates the plasma to bombard and react with the wafer. Due to the magnetic field, the inductive coupling method produces a very dense plasma. The ability to form very dense plasmas and, at the same time, control the ion bombardment of the substrate, enables ICP etching to have high etching rates with high mask selectivities.

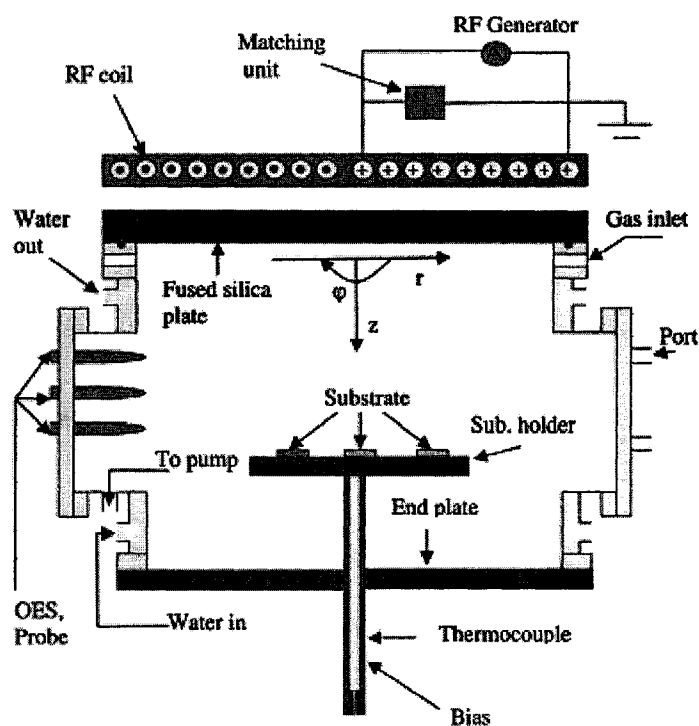


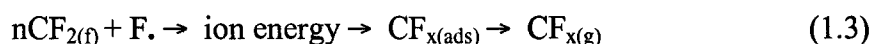
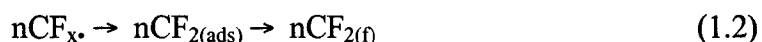
Figure 1.12 Sketch of an ICP coil chamber. The axial magnetic field induces an azimuthal electric field, which accelerates the charged particles [21].

There are different gas sources for etching different materials. Table 1 [22] lists the plasma etchants for common materials in microelectronics and microfabrication, such as Si, SiO₂, Si₃N₄, organics and aluminum.

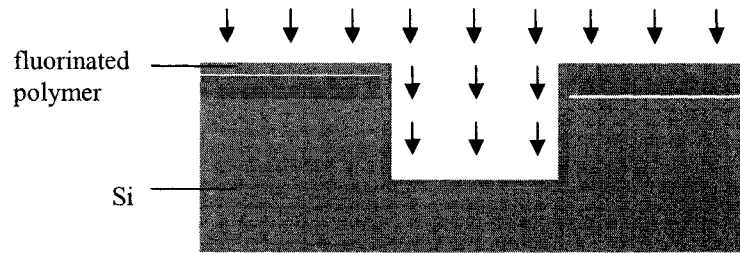
Table 1 Common materials and their plasma etchants in dry etching [22]

Materials to be Etched	Etchant gas
Si	CF ₄ , SF ₆
SiO ₂	CF ₄ /H ₂
Si ₃ N ₄	CF ₄ /O ₂
Organics	O ₂ , O ₂ / CF ₄ , O ₂ / SF ₆
Aluminum	BCl ₃

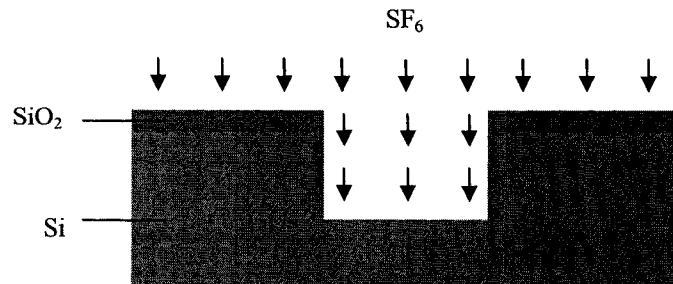
CF₄ and SF₆ have been generally used in Si plasma etching, as can be seen from Table 1. The chemical reaction for Si dry etching is shown in Equation 1.1, 1.2 and 1.3.



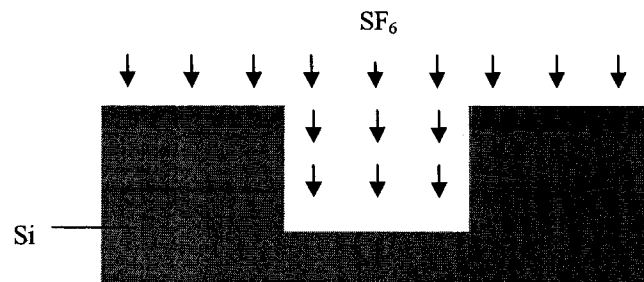
After CF₄ is admitted into the ICP system, it is dissociated into ions and radical species as shown in Equation 1.1. CF_x then goes through polymerization reactions to form nCF_{2(f)}, the passivation layer to be deposited on the sidewall and surface of the Si (Equation 1.2). Then, CF₄ is turned off and SF₆ gas is admitted, the dissociation of which would introduce fluorine radicals to remove the surface passivation layer (Equation 1.3). Figure 1.13 illustrates schematically the reactions occurring in the ICP system.



(a) Passivating layer is deposited on the surface of the silicon and the mask



(b) Fluorine radicals remove the surface passivation



(c) Fluorine radicals etch silicon

Figure 1.13 Schematic process of ICP etching system [23].

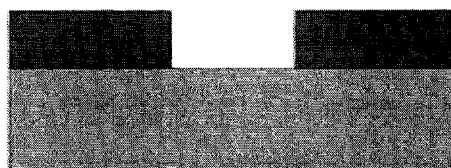
1.2.4 Metallization

Interconnections between devices and the outside world are realized by conductive films in microfabrication and microelectronics. Aluminum and gold are currently the two most widely used metals. The advantages of these metals are listed below. First of all, they are able to withstand high current densities without

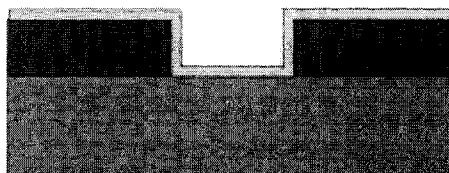
electromigration or material failure. Secondly, low-temperature deposition techniques are available for both aluminum and gold. Thirdly, they adhere to the substrate more easily. Fourthly, good ohmic contact can be made with aluminum and gold to both p- and n-type Si. Lastly, and most important of all, they are easy to be patterned and etched and are reliable throughout long-term operation. Gold is used in the fabrication discussed in this work.

Although gold can be etched in aqua regia ($\text{HCl}:\text{HNO}_3$ in a 3:1 ratio by volume), this approach is not desirable since it destroys most resist and metal mask materials. In industry, a commonly adopted way to etch gold is to use a dilution of KI and iodine in water. In the fabrication of the microbridge and microcoils, gold is patterned through a procedure called lift-off.

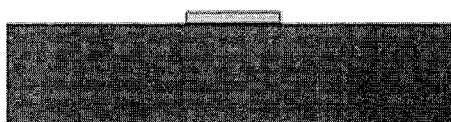
Lift-off is a simple and easy method for patterning metal thin films on a Si wafer surface. A simple schematic of the lift-off process is shown in Figure 1.14. The first step for lift-off is to pattern the wafer by standard lithographic techniques so that photoresist covers the regions where metal is not needed. By blanket-deposition of the desired metal over the entire substrate surface, including both photoresist covered areas and bare Si areas, a thin film of the metal is formed uniformly on the substrate. The metal thus contacts the substrate only in areas where it is needed. By soaking the wafer in a solvent to remove the photoresist, only the metal on the desired areas is left on the wafer surface while the rest of the metal is lifted off together with the photoresist beneath it. Ultrasonic is usually used during lift-off to promote the strip of the photoresist (and the metal above it) from the wafer substrate.



Wafer with patterned photoresist



Deposited metal



Strip photoresist and lift off unwanted metal

Figure 1.14 Lift-off procedure for patterning metal.

A potential problem with the lift-off procedure shown above is that the thin metal film deposited on the sidewall of the photoresist will stay on the substrate after the photoresist removal. The sidewall might be peeled off in subsequent processing, resulting in particulates and shorts on the substrate and affecting the processes that follow. An improved lift-off procedure is presented in Figure 1.15 by utilizing a two layer photoresist system with different etch rates. Since the etch rate for the bottom layer (usually LOR-7B) is faster than the top layer, the bottom photoresist is slightly undercut thus makes it easier to lift off the photoresist.

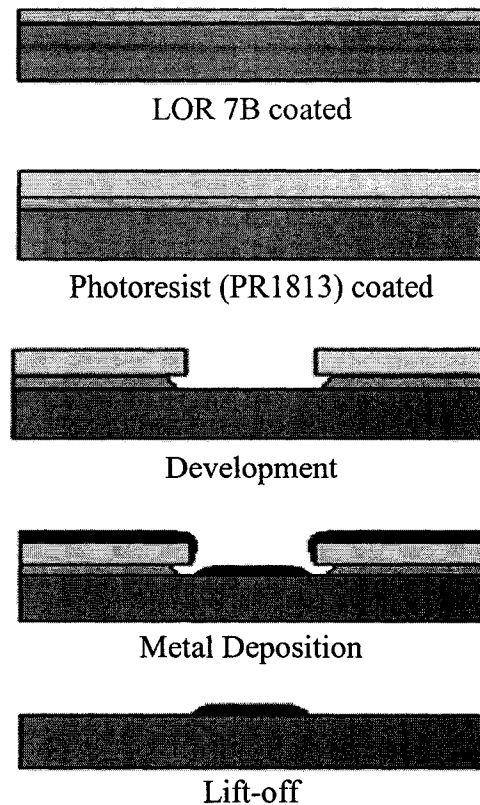


Figure 1.15 Improved lift-off with two-layers of photoresist and the bottom layer undercut.

1.2.5 Oxidation

SiO_2 has many applications in microfabrication and microelectronics. It can serve as a mask for diffusion and ion implantation, as a gate dielectric film, and as passivation layers, protecting the Si from contamination during subsequent processing steps. Upon exposure to air, the surface of Si is naturally oxidized and covered with a 15-20 Å thick layer of native SiO_2 .

During controlled oxidation, the Si wafers are placed in a furnace while oxygen gas (dry oxidation) or steam (wet oxidation) is flowing across them. In order to grow a layer of SiO_2 on a wafer in an acceptable amount of time the process has to be done at very high temperatures between 700°C and 1300°C. The thermal oxidation of Si

conducted in quartz furnace tubes allows relatively dense, adherent, trap-free layers of SiO₂ to be grown with ease.

Si is oxidized at its surface. The oxidizing species must therefore diffuse through the growing oxide layer in order to combine with the Si atoms at the wafer surface. The chemical reactions of Si with oxygen and water vapor are summarized respectively as shown in Equation 1.4 and Equation 1.5 below.



1.2.6 Thin Film Deposition

There are three primary ways for thin-film deposition, which are evaporation, sputtering and chemical vapor deposition. The following section discusses electron beam evaporation and sputtering, two deposition techniques used in the fabrication in this work.

The e-beam evaporator is used to evenly coat samples with metals. It is usually used when the required temperatures for the deposition of certain metals are too high for thermal evaporation. It is good for titanium, chrome, platinum or gold films deposition. In the evaporation process, the material (source) to be deposited is heated to the temperature where it liquefies and starts to evaporate. Then it is allowed to condense on the substrate. In a typical process the chamber is pumped down to a pressure of 5×10^{-6} torr to prevent air molecules from interfering with the deposition as well as allowing the molecules to evaporate freely from the source. A high-intensity electron beam gun (3 to 20keV) is focused on the source and causes the metal to evaporate and thus be deposited on the substrate. Typical deposition rates range from 1 to 5 Å/second. Figure 1.16

illustrates the schematic diagram of a typical e-beam evaporation system.

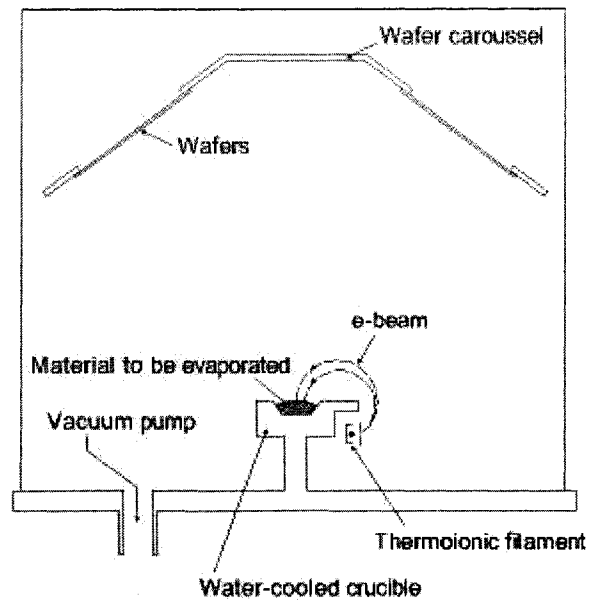


Figure 1.16 Typical e-beam evaporation system [24].

Sputtering is a technology in which the sputtered material is released from the source at much lower temperature than evaporation. It is more versatile than evaporation, and is extensively used in microfabrication. In a sputtering system, as shown in Figure 1.17 [25], the substrate is placed in a vacuum chamber with the source material, and an inert gas (such as argon) is introduced at low pressure. The gas is ionized using an RF power source. The ions are accelerated towards the surface of the target, causing atoms of the source material to be ejected from the target and deposited on the substrate.

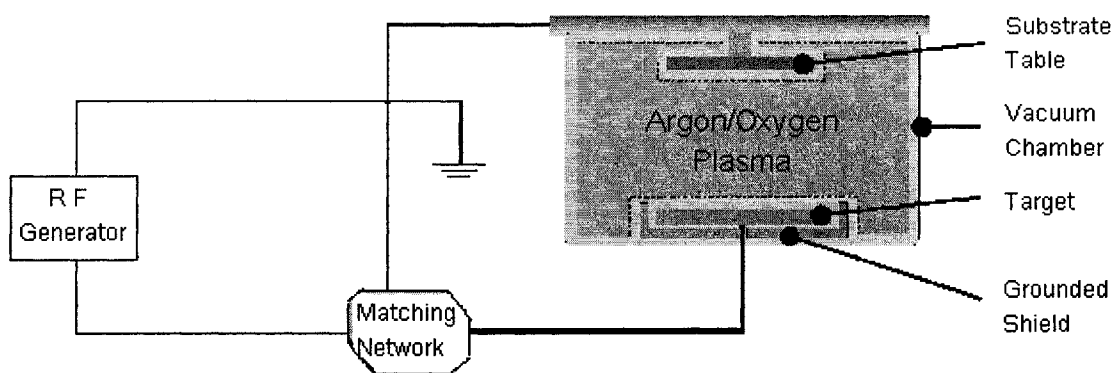


Figure 1.17 The principle of a sputtering system [25].

1.3 Research Objectives

Design and fabrication of highly sensitive chemical and biological sensors is of great interest to a number of researchers. There are still enough opportunities for microsensors to be improved with optimized structures, enhanced sensitivity and new materials, as well as enhanced performance.

The objective of this research is to design and develop new chemical and biological sensors based on Si microfabrication technologies. Specifically, piezoresistive microbridges and microcoils have been selected as the microsensors to be designed and fabricated due to their high sensitivity and stability. The materials used for the fabrication of the microsensors were Si, SiO₂ and SU-8. Before the fabrication, the microsensors were simulated via Finite Element Analysis software to determine the optimized size and design for the structures. Standard Si fabrication techniques, including spin-coating, lithography, wet and dry etching and lift-off, were used to fabricate the microsensors. After the fabrication, the sensors were characterized by exposing them to a real environment to test their performance.

1.4 Dissertation Outline

There are six chapters in this dissertation. The first chapter overviews chemical and biological sensors and their applications followed by an introduction to the microfabrication technologies as well as the objective of this dissertation. The second chapter describes the materials used in the fabrication of the microsensors and the measurement instruments and techniques for device characterization. Chapter three focuses on the simulation, fabrication and characterization of the microbridge sensors. Chapter four describes the principle, the fabrication and the characterization of the microcoil sensors. Chapter five is focused on a new approach to grow gold and platinum nanowires. The last chapter concludes this dissertation and discusses the prospects for future work that still needs to be done.

CHAPTER TWO

EXPERIMENTAL MATERIALS

AND EQUIPMENTS

Si is the most widely used material in microfabrication. Si and its physical properties are the basis for subsequent microfabrication processing. This chapter presents the structure of Si and its corresponding properties. Other materials used in this work, including SU-8, PDMS, Shipley 1813 are also introduced. The principles of metrology instruments used for device characterization, including SEM, AFM, and surface profilometer, are briefly discussed in this chapter.

2.1 Experimental Materials

2.1.1 Si

Si is so far the most widely used material for microfabrication and microelectronics. A brief introduction on the atomic structure of Si and its physical properties would help to understand the corresponding fabrication techniques and the physics of Si devices.

Si is a crystalline solid. Its atoms are organized in an orderly array, as shown in Figure 2.1. The diamond lattice structure, the smallest assembly of atoms that can be repeated to form crystalline Si is called the unit cell.

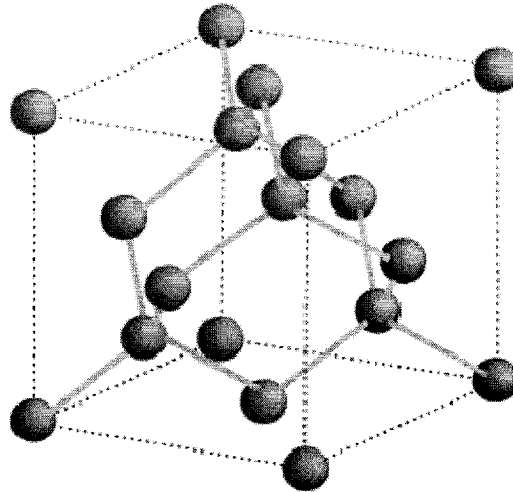


Figure 2.1 Diamond unit cell of Si [25].

Piezoresistivity is a very important property of Si. It has been reported that the resistivity of a material depends on the internal atom positions and their motions [26]. By applying strain or stress to a material, the atomic positions of the material would be changed. This change would cause the energy band to shift compared to the stress-free state. Thus, in some directions of the material, the resistivity would be larger while in other directions the resistivity would be smaller. The overall resistivity of the material will change after a strain or stress is applied and the change of the resistivity is related to the magnitude of the applied strain or stress. More details of the piezoresistive properties of Si will be covered in chapter 3. The designs of the microbridge and microcoil sensors are all based on the piezoresistive property of Si.

2.1.2 SU-8

SU-8 is used in the fabrication of the microcoil, standing side by side with the Si microcoil. SU-8 is a high contrast, epoxy based negative photoresist designed for micromachining and other microelectronic applications. High aspect ratios larger than

10:1 with near vertical side walls can be attained by using SU-8. After crosslinking, SU-8 is very stable, highly resistant to solvents, acids and bases, which make it a good choice for permanent use applications.

There are a series of products in the SU-8 family including 2-25, 50-100, 2000 and 3000 depending on the viscosity. SU-8 50 is selected for its desired viscosity (12250 cst @ 25 °C) to fabricate the microcoils in this dissertation. The standard process procedures for SU-8 are listed in Figure 2.2.

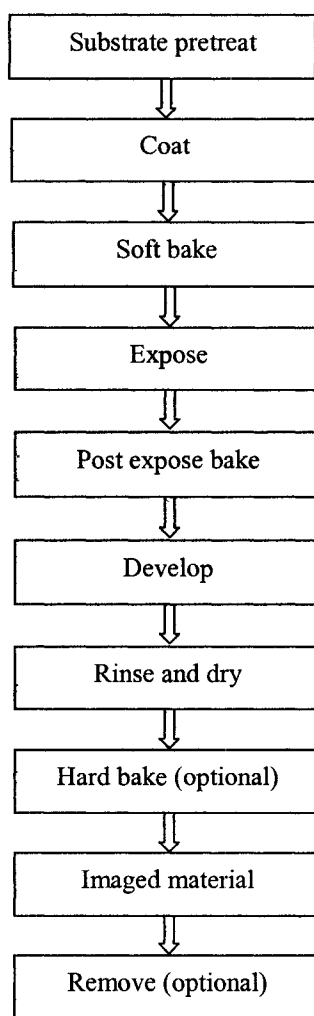


Figure 2.2 Standard process procedures for SU-8 [27].

Prior to spin-coating SU-8 on the Si wafer, the surface of the wafer should be cleaned by acetone spray to remove organic contaminants. Then the wafer should be dried on a hot plate at 500 °C for 5 minutes.

The spin-coating recipe, as illustrated in Figure 2.3, is adopted to obtain a 50 μm thick SU-8 film. The spinner is first ramped to 500 rpm at 100 rpm/second acceleration. This speed is held for 5 seconds to allow the resist to cover the entire surface. Then the spinner is ramped to the final speed of 1000 rpm at an acceleration speed of 300 rpm/second and held for a total of 40 seconds [27].

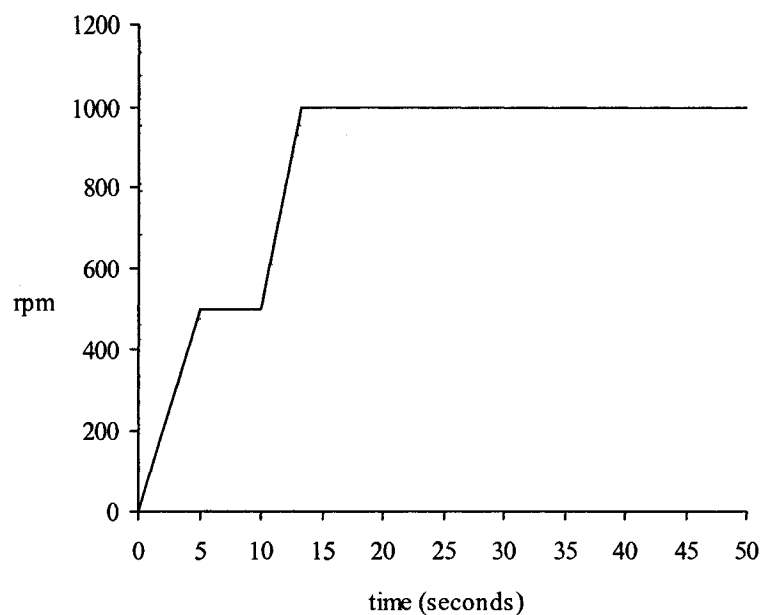


Figure 2.3 Spin-coating recipe for SU-8.

The next step is soft bake, the purpose of which is to evaporate the solvent and densify the film. Soft bake is conducted at 65 °C for 10 minutes and then stepped to 95 °C for 30 minutes. The stepped soft bake temperatures are used to allow the solvent to

evaporate from the film at a more controlled rate thus achieving better coating uniformity, reduced edge bead and better resist-to-substrate adhesion [27].

After soft bake, the SU-8 thin film is exposed to near UV (365nm) exposure for 50 seconds. Underdevelopment would cause the desired SU-8 to be etched away while overdevelopment would result in problems in development.

Following exposure, post exposure bake must be performed to further cross link the exposed portions of the film. As with soft bake, post bake is also performed using a stepped temperature cycle. The reason this is done is to minimize film stress and resist cracking problems. One minute bake at 65 °C is followed by an 8 minute bake at 95 °C for 50 μm thick SU-8 film.

After post exposure bake, the wafer, covered with SU-8 film, should be soaked in SU-8 developer to dissolve away non-exposed SU-8 and selectively leave crosslinked SU-8 on the wafer. This procedure, in practice, lasts for about 6 minutes for 50 μm thick SU-8.

Subsequent processing steps include rinsing the wafer with isopropyl alcohol (IPA) to remove resist residue, rinsing the wafer with DI water to clean the wafer, blowing dry the wafer with nitrogen gas and an optional hard bake at 200 °C to further crosslink the SU-8.

The SU-8 used in the fabrication of the microcoil in this dissertation is commercially available from Microchem.

2.1.3 PDMS

Polydimethylsiloxane (PDMS) is widely used as a Si-based organic polymer, and is known for its unusual flow properties. It is optically clear, very viscous, inert,

non-toxic and non-flammable. Standard PDMS process procedures are listed in Figure 2.4.

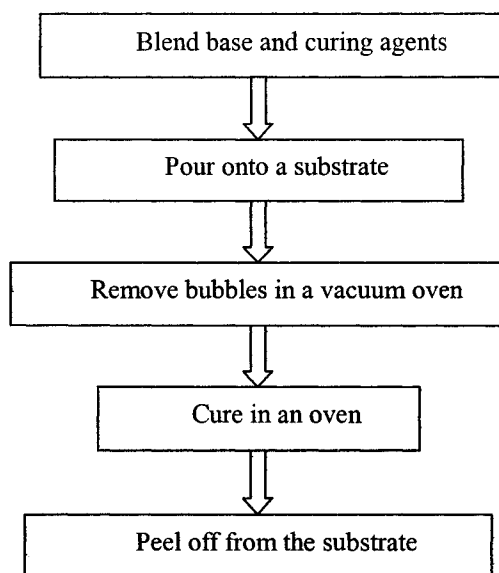


Figure 2.4 Standard PDMS process procedures.

SYLGARD 184 was purchased from Dow Corning (Midland, MI). SYLGARD 184 consists of a “base” (prepolymer) and “curing agent” (crosslinker) that need to be mixed thoroughly at a 10:1 w/w ratio. After the base and the curing agent are mixed and then transferred onto a substrate such as a Si wafer, they are degassed in a vacuum oven for 30 minutes to remove any bubbles generated during mixing. Then PDMS is cured at 95 °C for 2 hours or overnight at 60 °C. The last step is to peel off the PDMS from the substrate after the PDMS is cooled down to room temperature. Care must be taken to keep the PDMS film from being torn. The thickness of the PDMS obtained following above procedures is around 500 μm . By using a container to encase the substrate and prevent the PDMS from flowing off the substrate, thicker PDMS can be obtained.

2.1.4 PR1813

Shipley 1813 positive tone photoresist (PR1813) has been widely used as a positive photoresist for pattern transfer from the mask to the wafer. It is UV curable and solvent soluble, and very easy to handle. To spin coat PR1813 onto a wafer, the following steps are followed,

- First, center the wafer on the spinner.
- Second, transfer PR1813 from the container to the wafer with a pipette.
- Third, ramp the spin coater first to 1000 rpm at 100 rpm/second acceleration. Hold at this speed for 10 seconds to allow the resist to cover the entire wafer surface.
- Fourth, ramp the spin coater to 3000 rpm at 500 rpm/second acceleration. Hold at this speed for a total of 40 seconds. Figure 2.5 shows the spin-coating recipe for PR-1813.
- Fifth, soft bake the wafer at 110 °C for 1 minute to evaporate the solvent and dry the film.
- Sixth, expose the wafer to UV light through a mask for 8 seconds.
- Seventh, develop the wafer in Microposit Developer for about 45 seconds. Inspect the pattern frequently during the development to see if it is etched properly.
- Eighth, bake the wafer at 115 °C for 1 minute to further dry the film and prevent reflowing.

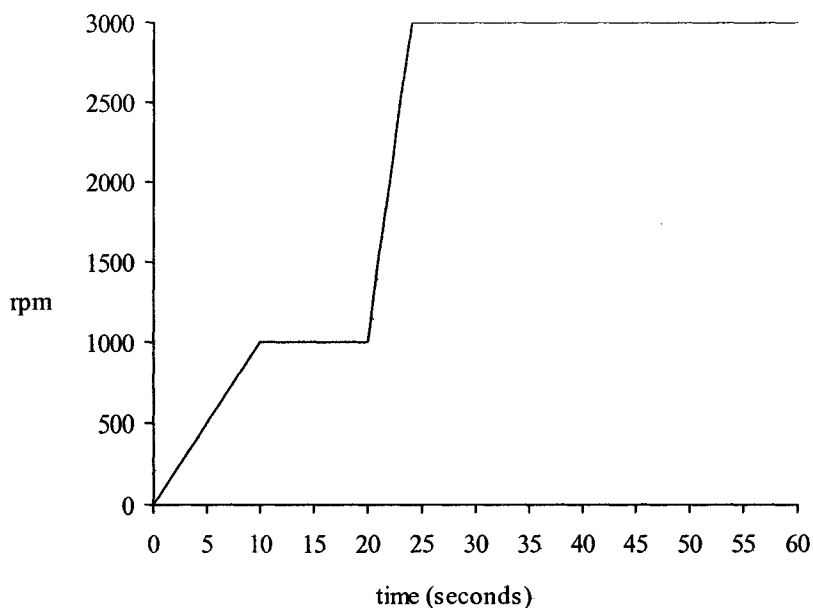


Figure 2.5 Spin-coating recipe of PR 1813.

2.2 Experimental Equipment

2.2.1 SEM

Compared to an optical microscope which utilizes visible light to create magnified images of a sample surface, the scanning electron microscope (SEM) is an electron microscope using electrons to produce high-resolution images. The images taken by SEM have a characteristic three-dimensional appearance and can show very detailed information of the sample surface.

In the SEM, electrons are emitted from the cathode and are accelerated towards the anode. When the primary electron beam interacts with the sample, the electrons lose energy and generate secondary electrons, backscattered electrons, and characteristic X-rays. By detecting these signals, images on the sample surface can be formed and

displayed on a cathode ray tube screen. Features as small as 5 nm can be detected by SEM.

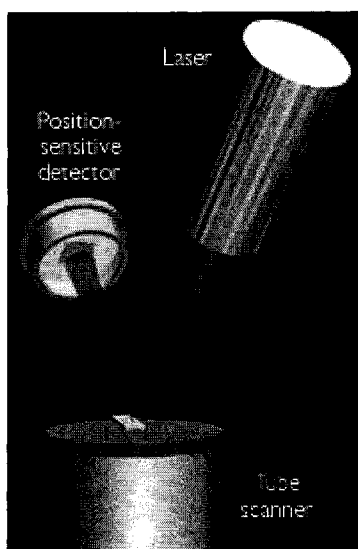
Figure 2.6 illustrates the SEM (Amray 1830) used for this work. It has two major parts, the electron optical column console and the electronics and display console.



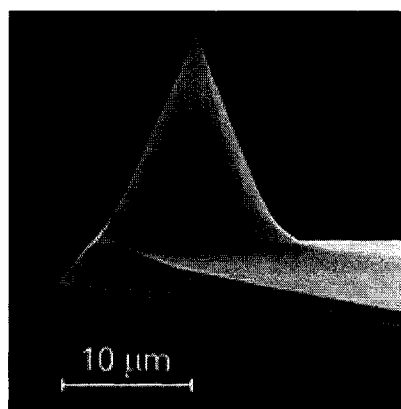
Figure 2.6 Amray 1830 SEM.

2.2.2 AFM

The atomic force microscope (AFM) uses a sharp probe to detect surface features on a sample. It is possible to image the surface topography of an object with extremely high resolution with the AFM. A schematic of the principle of operation of the AFM is shown in Figure 2.7 [28].



(a)



(b)

Figure 2.7 (a) Operating principle of the AFM and (b) the tip of the AFM [28].

The key part of the AFM is a small microcantilever with a very sharp tip at the end (Figure 2.7 (b)). When the tip scans over the surface of a sample, interatomic forces between the cantilever tip and the sample surface cause the cantilever to be deflected as the surface topography of the sample changes. This deflection causes a deflection of the laser beam, which is reflected off the cantilever beam, and is detected by a photodetector. Thus, any change in the surface topography is converted into electrical signals and a map of the sample topography can be generated.

The advantage of the AFM is that it provides a true three-dimensional surface profile of a sample, and it can, in principle, provide higher resolution than the SEM.

2.2.3 Surface Profilometer

Step height needs to be checked from time to time during the process of microfabrication. A profilometer works to fulfill this purpose. A profilometer usually has a diamond stylus that scans over the surface of the sample. A surface profile over a specified range could be generated by recording the displacement of the diamond stylus versus the position scanned. Step heights and surface roughness of the sample substrate can be determined from the profile. Figure 2.8 shows the profilometer used for this work (KLA Tencor Profilometer).

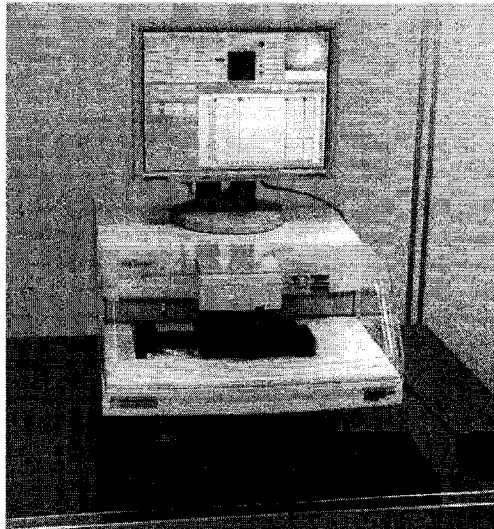


Figure 2.8 KLA Tencor profilometer.

CHAPTER THREE

SIMULATION AND FABRICATION

OF MICROBRIDGES

3.1 Introduction

Advances in the field of micro- and nano-electro-mechanical systems (MEMS and NEMS) now offer unique opportunities in the design of small and ultrasensitive micro sensors. Microcantilevers have proven to be an outstanding platform for chemical and biological sensors. The unique characteristic of microcantilevers is that the device can be made to undergo bending due to molecular adsorption by confining the adsorption to one side of the cantilever. This bending is due to adsorption-induced differential stress on the cantilever.

The challenge associated with the microcantilever is the stability of the cantilever when the device is used on a mobile vehicle or moving object. It appears that a microbridge device will overcome the stability problem associated with the microcantilever. A microbridge can be considered as the head-to-head fusion of two cantilevers where the middle of the bridge would deform in a way similar to a microcantilever due to molecular adsorption upon exposure to the analyte (Figure 3.1(a)).

It is anticipated that this microbridge sensing device will be more stable than the microcantilever, especially in turbulent or vibrant conditions. The trade-off might be the low $\Delta R/R$ change of the microbridge compared to that of the microcantilever.

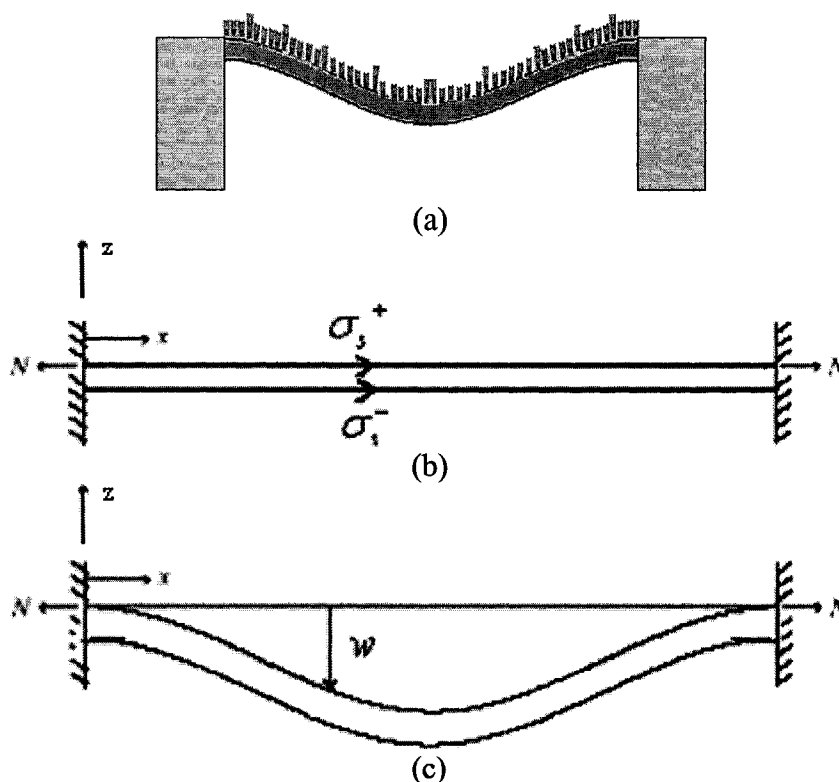


Figure 3.1 (a) Schematic of the bending of a microbridge due to analyte adsorption; (b) the microbridge under the effect of net surface stress $\Delta\sigma$, due to physical adsorption on the bridge surface and (c) the resultant arcuation of the bridge in z direction.

Microbridges, based on the principle of electrostatic excitation and capacitive detection, have been used as integrated chemical vapor sensors for sensing gas composition of binary mixtures [29] - [33]. Various transduction mechanisms have been developed to detect the resonance frequency changes of microbridges. These mechanisms include the piezoresistive approach based on polysilicon piezoresistors [33] - [38], the piezoelectric approach with piezoelectric (PZT) materials, such as ZnO [39] - [41], and

the optical approach using laser light to measure the frequency change or displacement movement [42] - [44]. These microbridges are sensitive transducers that provide the basis for mass [45] - [47], temperature [48], [49], strain [50], acceleration [51], and vibration sensors [52].

Microbridges have been fabricated from Si [34], [36] - [38], [46], [53] - [55], silicon carbide [56], [57], silicon nitride [58], metals [59], [60], metal composites [61], and polymers [62], [63]. Resonant microbridge sensors made of polysilicon have been simulated and fabricated using typical micromachining techniques and integrated with on-chip electronics using CMOS [64] - [66].

Most of these devices took advantage of the fact that the resonance frequency of microbridge and nanobridge structures was in the ultrasonic and MHz range, as compared to the KHz range of microcantilevers [67], [68]. Few publications have reported using the arcuation of the microbridge for developing chem/biosensors although the arcuation of microbridges has been used for testing young's modulus and residual stress of thin bilayer films [69]. We expected that materials with a smaller young's modulus would be appropriate for developing chem/biosensors based on the arcuation of microbridge sensors due to the changes of adsorption-induced surface stress. Among those materials with really small Young's modulus, we are especially interested in SiO₂, whose Young's modulus is 76.5-97.2 GPa, which is half of that of Si. One of our considerations is that the SiO₂ microbridge can be readily fabricated by using a traditional photolithographic process. Furthermore, such an SiO₂ microbridge may be extremely useful in detection of HF and nerve agents, according to our previous study on SiO₂ microcantilevers [70].

Different methods can be used to measure the arcuation of the microbridge induced by surface stress changes. It is our perception that the piezoresistive microbridge will be most suited for developing a hand-held sensor device. In this work, we investigate the simulation and fabrication of SiO_2 microbridges with piezoresistive Si on the microbridge.

There have been several reports on simulation and design of resonant microbridges [41], [70], [71], but no work has been done on simulation of piezoresistive and SiO_2 based microbridges. This work uses a popular finite element analysis approach to simulate the geometrical parameters for SiO_2 microbridges. A thin layer of boron doped Si on the SiO_2 surface was used as the piezoresistive material. A Finite Element Model was developed to analyze the electrical and mechanical response of piezoresistor cantilevers by using CoventorWare (Coventer Inc. Cary, NC). The fabrication process of a Si covered SiO_2 microbridge is reported.

3.2 Finite Element Model

Computer Aided Engineering (CAE) is the application of computer software in engineering to evaluate components and assemblies. It encompasses simulation, validation and optimization of products and manufacturing tools. The primary application of CAE, used in civil, mechanical, aerospace, and electronic engineering, takes the form of FEA alongside Computer Aided Design (CAD).

Finite Element Analysis (FEA) is a computer simulation technique used in engineering analysis. It uses a numerical technique called the finite element method (FEM). In general, there are three phases in any computer-aided engineering task, which are pre-processing, analysis solver and post-processing of results.

The first step in using FEA, which is pre-processing, is constructing a finite element model of the structure to be analyzed. The input of a topological description of the structure's geometric features is required in most FEA packages. This can be in either 1D, 2D or 3D form, modeled by lines, shapes or surfaces representation respectively, although nowadays 3D models are predominantly used. The primary objective of the model is to realistically replicate the important parameters and features of the real model. The simplest mechanism to achieve modeling similarity in structural analysis is to utilize pre-existing digital blueprints, design files, CAD models and/or data by importing that into the FEA environment. Once the finite element geometric model has been created, a meshing procedure is used to define and break the model up into small elements. In general, a finite element model is defined by a mesh network, which is made up of the geometric arrangement of elements and nodes. Nodes represent points at which features, such as displacements, are calculated. FEA packages use node numbers to serve as an identification tool in viewing solutions in structures, such as deflections. Elements are bounded by sets of nodes and define the localized mass and stiffness properties of the model. Elements are also defined by mesh numbers which allow reference to be made to corresponding deflections or stresses at specific model locations.

The next stage of the FEA process is analysis. The FEM conducts a series of computational procedures involving applied forces and the properties of the elements, which produces a model solution. Such a structural analysis allows the determination of effects such as deformations, strains, and stresses which are caused by applied structural loads, such as force, pressure and gravity.

These results can then be studied using visualization tools within the FEA environment to view and to fully identify the implications of the analysis. Numerical and graphical tools allow the precise location of data, such as stresses and deflections, to be identified.

We used p-type boron doped Si piezoresistors for the simulation in this work since p-type piezoresistors have a larger sensitivity than n-type piezoresistors. Finite element analysis is performed using a specially designed piezoresistive solver of the CoventorWare software.

CoventorWare is a very powerful FEA based MEMS simulation software. It can be used to simulate on mechanics, fluidics, electrostatics and inductance. Among its various modules, MemMech and MemPzr are the two that have been used in this dissertation. Figure 3.2 is the flowchart using CoventorWare to design and simulate MEMS system.

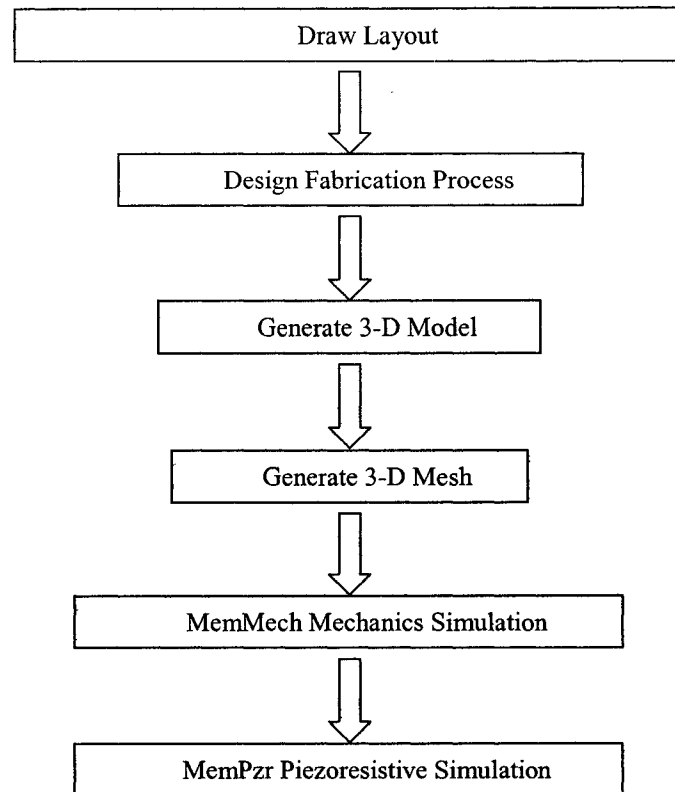


Figure 3.2 Flowchart of CoventorWare simulation process.

Based on the schematic design shown in Figure 3.3, the mesh model for the SiO_2/Si based piezoresistive microbridge was constructed.

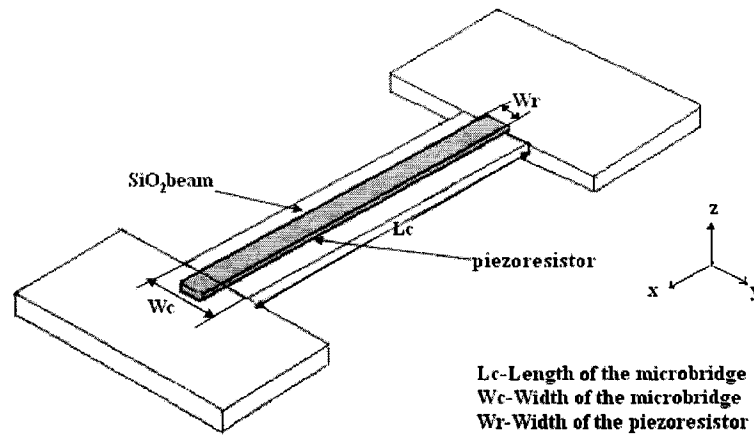


Figure 3.3 Schematic model of a Si covered SiO₂ microbridge.

The arcuation change of a microbridge is illustrated in Figure 3.1 (c). Figure 3.1 also illustrates boundary conditions when surface stresses are applied to the microbridge. The arcuation due to surface stress is modeled using the MemMech solver that is coupled to the piezoresistive solver for simulating the sensor response of arcuation based piezoresistive microbridges. In order to obtain the numerical solution for the piezoresistive effect, the solver uses ohms law in the stress-free state as shown in Equation (3.1):

$$\begin{bmatrix} E_1 \\ E_2 \\ E_3 \end{bmatrix} = \rho_0 \begin{bmatrix} 1 & 0 & 0 \\ 0 & 1 & 0 \\ 0 & 0 & 1 \end{bmatrix} \begin{bmatrix} i_1 \\ i_2 \\ i_3 \end{bmatrix} \quad (3.1)$$

where E_i , i_i are the electric field and current density, respectively, parallel to the x_i crystallographic axis and ρ_0 is the stress-free resistivity. It was previously reported [72] that the application of differential surface stress onto a rectangular plate was equivalent to the loading of the free edges by moments per unit length of magnitude $\Delta\sigma/2$. When

applying the boundary conditions for the meshed model, the above result was taken into consideration.

The application of surface stress causes the microbridge resistivity to change. The change in resistivity is related to the stress tensor through the empirically determined piezoresistive coefficient. For the Si material, there are three independent piezoresistive coefficients π_{11} , π_{12} , and π_{44} , where the subscripts physically represent the electrical field, current density, and stress along the three crystallographic directions for cubic crystal Si. The properties of materials (Si and SiO₂) used in this work are listed in Table 2 and Table 3 respectively [73].

Table 2 Material properties of Si with surface stress at [110] direction used in the simulation

Material Property	Material property of Si with surface stress at [110] direction
Young's modulus (MPa)	1.30×10^5
Poisson's Ratio	0.278
Shear Modulus (MPa)	7.96×10^4
Density (kg/m ³)	2.33×10^3
Thermal coefficient (pW/umK)	1.48×10^8
Resistivity (Ω -cm)	7.8

Table 3 Material properties of SiO₂ used in the simulation

Young's Modulus (MPa)	7.0×10^4
Poisson's Ratio	0.17

In the simulation, the two ends of the bridge were fixed and the mesh size in the x, y, z directions were 2 μ m, 2 μ m, and 0.2 μ m, respectively, which assures the error to be within 0.01%. A 2 N/m surface stress and 300 K temperature were applied to the microbridge for simulation.

3.3 Results and Discussion

In the simulation, the surface stress is applied on the top surface of the microbridge, as shown in Figure 3.1. The boundary conditions include a surface stress of 2 N/m and a temperature of 300K. A 2 N/m surface stress was used in this study because the surface stress changes at this level have been observed in many chemical and biological sensors.

3.3.1 Effect of thickness of piezoresistor on the microbridge arcuation and fractional change in resistance of the microbridge ($\Delta R/R$)

When the Si piezoresistor thickness decreases, the physical consequence to the thin piezoresistor is the confinement of charge carriers in the direction perpendicular to the bridge surface. From our simulation, we observed that any decrease in piezoresistor thickness cause an increase in the fractional change in the resistance of the microbridge ($\Delta R/R$). Figure 3.4 (a) shows that the decrease in thickness from 2 μm to 0.2 μm causes approximately a 16-fold increase in the $\Delta R/R$ response. Variations were observed for various widths of the Si piezoresistor. The decrease in width from 10 μm to 2 μm caused the $\Delta R/R$ response to increase by 25% to 300%, depending on the thickness of the piezoresistors. The thickness of the piezoresistor has a more significant affect on the sensor signals than that of the width. When the Si is as thin as 0.2 μm , the $\Delta R/R$ is not affected as much by the width of the Si piezoresistor.

The arcuation variation of the piezoresistive microbridge, as a function of the width and thickness of the microbridge, have a very similar profile, as shown in Figure 3.4 (b). The $\Delta R/R$ change as a function of the arcuation variation is shown in Figure 3.4 (c). These results indicated that the resistance change of the bridge under surface stress is

nearly directly proportional to the arcuation change, especially when the arcuation was larger than $0.3 \mu\text{m}$. The significant $\Delta R/R$ signal for thinner and narrower piezoresistor covered microbridges may be mainly due to the greater arcuation of those microbridges.

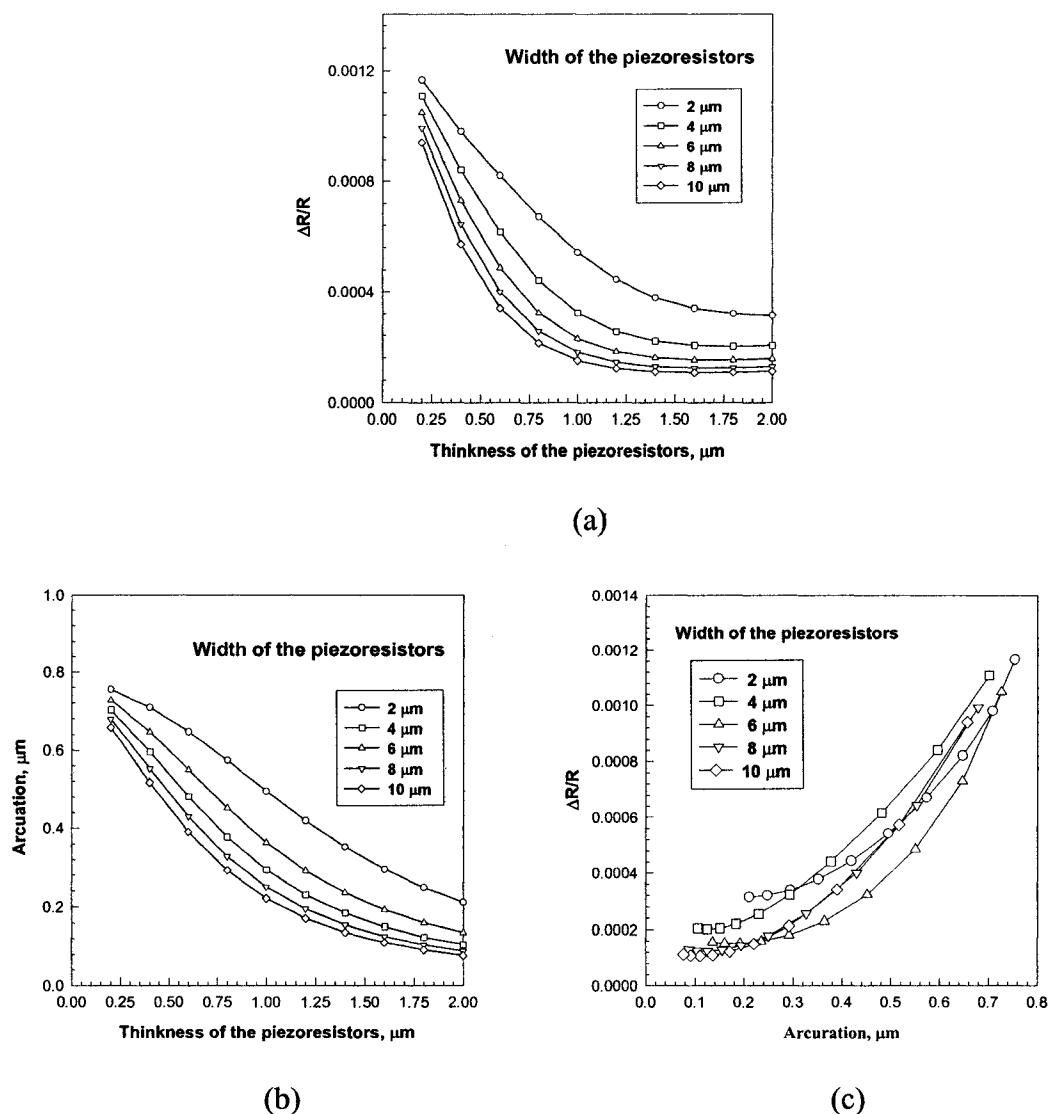
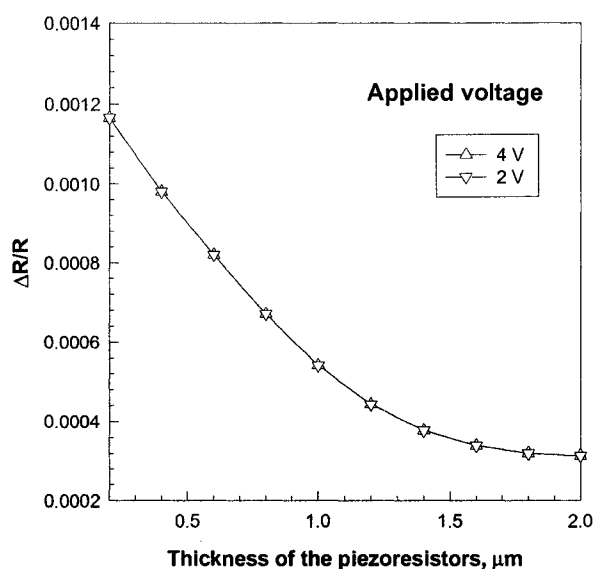


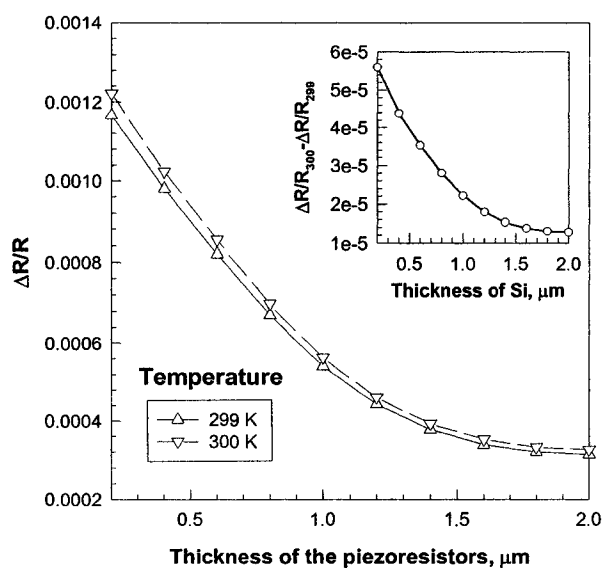
Figure 3.4 The (a) $\Delta R/R$ and (b) arcuation of SiO_2 microbridge vs. the thickness of Si piezoresistor on the microbridge, when a surface stress of 2 N/m was applied on the surface of SiO_2 microbridge. c) $\Delta R/R$ vs. the arcuation of the SiO_2 microbridge. The dimensions of the SiO_2 microbridges were $400 \mu\text{m}$ in length (L_c), $50 \mu\text{m}$ in width (W_c), and $1 \mu\text{m}$ in thickness. The Si piezoresistors were $400 \mu\text{m}$ in length (L_p) and width varying from $2 \mu\text{m}$ to $10 \mu\text{m}$. The doping concentration is $1 \times 10^{17} \text{ cm}^{-3}$.

It has been reported that the $\Delta R/R$ change is directly proportional to the microcantilever bending [74]. Our simulation results suggest that a similar relationship could be used to correlate the $\Delta R/R$ change with arcuation of the microbridges, although no equations have been developed in the literature.

The $\Delta R/R$ keeps increasing when the thickness decreases. The optimized thickness for chem/bio sensing, however, will be obtained from noise optimization. Piezoresistive sensors have two main possible noise sources, thermal and Hooge noise, which are generated from temperature and voltage variations, respectively [75]. Larger noise will lower the signal/noise (S/N) ratio, and thus the sensitivity. The S/N ratio under temperature and voltage variations could be used to optimize the thickness of the piezoresistive microbridge. Figure 3.5 (a) shows that a 100% voltage variation does not change the $\Delta R/R$ of the microbridge. However, a 0.3% temperature variation, as shown in Figure 3.5 (b), generates significant noise, especially when the Si piezoresistor is thinner than $1 \mu\text{m}$. Figure 3.5 (b) inset shows the resistance change noise due to the 0.3% temperature variation (defined as $\Delta R / R_{300K} - \Delta R / R_{299K}$). The thermal noise of the resistors increased approximately 5-fold when the thickness decreases from $2 \mu\text{m}$ to $0.2 \mu\text{m}$.



(a)



(b)

Figure 3.5 Effect of (a) voltage variation, (b) temperature variation on the $\Delta R/R$ change of microbridges with different thicknesses. The SiO_2 microbridges were $400 \mu\text{m}$ in length, $50 \mu\text{m}$ in width, and $1 \mu\text{m}$ in thickness. The piezoresistors were $400 \mu\text{m}$ in length, $2 \mu\text{m}$ in width, with the thickness varying from $0.2 \mu\text{m}$ to $2 \mu\text{m}$. The doping concentration is $1 \times 10^{17} \text{ cm}^{-3}$.

From those data in Figure 3.5 (b) and Figure 3.5 (b) inset, the S/N ratio of the microbridges at different thicknesses were calculated and shown in Figure 3.6. These results suggest that although the $\Delta R/R$ of the microbridge increases when the thickness decreases, the S/N ratio does not change significantly from 2 μm to 0.2 μm thickness, i.e. when the temperature variation is controlled to 1 K, the thickness of the Si piezoresistor does not play a critical role in obtaining the best S/N ratio.

When simulated and compared to microcantilevers with the same dimensions, the $\Delta R/R$ change of the microbridge is approximately 1/3 of that of the microcantilever, and the microbridge is approximately 50% more temperature dependent than the microcantilever.

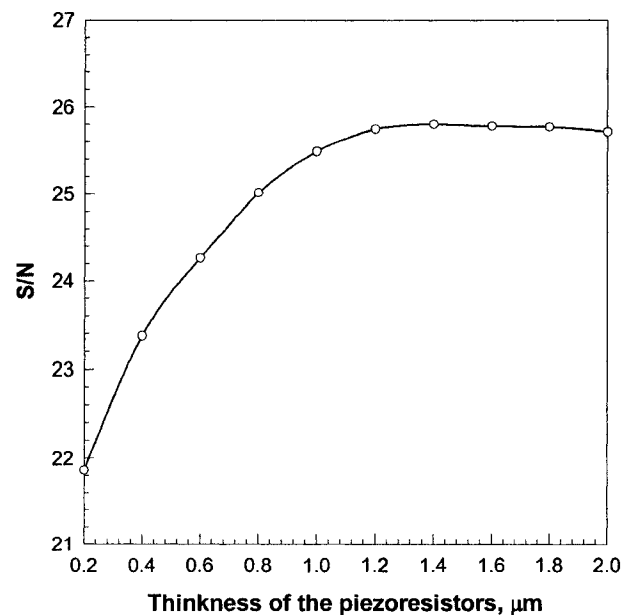


Figure 3.6 S/N ratio of microbridges with the thickness of the piezoresistor varying from 0.2 μm to 2 μm . The SiO_2 microbridges were 400 μm in length, 50 μm in width, and 1 μm in thickness. The piezoresistors were 400 μm in length and 2 μm in width. The doping concentration is $1 \times 10^{17} \text{ cm}^{-3}$.

3.3.2 Effect of doping concentrations of the piezoresistor on the $\Delta R/R$ changes

The resistance change of a piezoresistor ($\Delta R/R$) after a stress is applied can be expressed as shown in Equation 3.2.

$$\frac{\Delta R}{R} = \pi_l \sigma_l + \pi_t \sigma_t \quad (3.2)$$

where R is the resistance of the stress-free piezoresistor, π_l , σ_l and π_t , σ_t refer to the piezoresistive coefficient and stress along the longitudinal and traverse direction with respect to the resistor axis, respectively.

π_l and π_t can be expressed as follows,

$$\begin{aligned} \pi_l &= \pi_{11} - 2(\pi_{11} - \pi_{12} - \pi_{44})(l_1^2 m_1^2 + l_1^2 n_1^2 + m_1^2 n_1^2) \\ \pi_t &= \pi_{12} + (\pi_{11} - \pi_{12} - \pi_{44})(l_1^2 l_2^2 + m_1^2 m_2^2 + n_1^2 n_2^2) \end{aligned} \quad (3.3)$$

where (l_1, m_1, n_1) and (l_2, m_2, n_2) are the sets of direction cosines between the longitudinal resistor direction and the crystal axis, and between the transverse resistor direction and the crystal axes [76].

For piezoresistors oriented along the [110] direction in (100) wafers, (l_1, m_1, n_1) and (l_2, m_2, n_2) are $(1/\sqrt{2}, 1/\sqrt{2}, 0)$ and $(-1/\sqrt{2}, 1/\sqrt{2}, 0)$ respectively. Inserting these values into Equation (3.3), we have,

$$\begin{aligned} \pi_l &= \frac{1}{2}(\pi_{11} + \pi_{12} + \pi_{44}) \\ \pi_t &= \frac{1}{2}(\pi_{11} + \pi_{12} - \pi_{44}) \end{aligned} \quad (3.4)$$

Since the length of the microbridge is much longer than its width and the surface stress is along the x axis, the microbridge can be seen as a 1-D device and Equation (3.2) could be reduced to Equation (3.5)

$$\frac{\Delta R}{R} = \pi_l \sigma_l \quad (3.5)$$

At low doping concentrations ($< 5 \times 10^{14} \text{ cm}^{-3}$), the piezoresistive coefficient in the [110] direction for p-type Si is a constant at $72 \times 10^{-11} \text{ m}^2 / \text{N}$ [76]. Numerous reports showed that when the doping concentration is increased, the piezoresistive coefficient π_l is decreased [77]. The model developed by Kanda [78] is accurate only for low doping concentrations. A piezoresistive factor $P(p)$ was defined to express the coefficients as a fraction of this maximum value by the approximation Equation (3.6) for concentration above 10^{17} cm^{-3} .

$$P(p) = \text{Log} \left(\frac{b}{p} \right)^a, \quad (3.6)$$

where $a = 0.2014$, $b = 1.53 \times 10^{22} \text{ cm}^{-3}$ and p is the doping concentration.

The Piezoresistive factor $P(p)$ is directly related to π_l by Equation (3.7) [15].

$$\pi_l(N, T) = P(p) \pi_l(300K), \quad (3.7)$$

The above logarithmic equation predicts that π_l decreases 9.7% when the doping concentration is increased from 10^{17} cm^{-3} to $5 \times 10^{17} \text{ cm}^{-3}$, 22.2% when the concentration is increased from $5 \times 10^{17} \text{ cm}^{-3}$ to $5 \times 10^{18} \text{ cm}^{-3}$, and 28.7% when the concentration is increased from $5 \times 10^{18} \text{ cm}^{-3}$ to $5 \times 10^{19} \text{ cm}^{-3}$. Since π_l is directly related to $\Delta R/R$ from Equation (3.5), it is expected that the $\Delta R/R$ change will be affected by changes in doping concentrations. The profiles of $\Delta R/R$ vs. doping concentration

(Figure 3.7) were similar, confirming a good agreement with theoretical predictions. Relatively lower doping concentration (10^{17} cm^{-3}) will be used in our fabrication in order to obtain higher $\Delta R/R$ response.

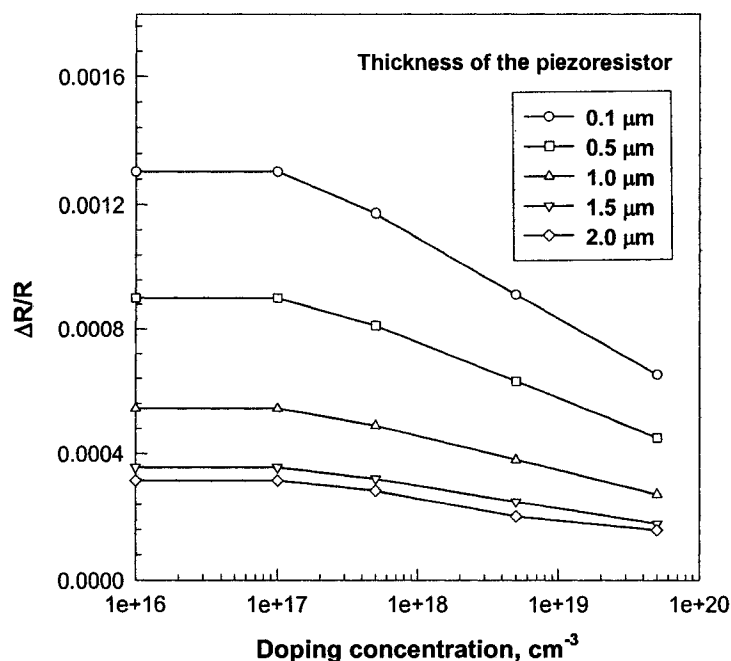


Figure 3.7 The $\Delta R/R$ vs. doping concentration when a 2 N/m surface stress is applied on the surface of an SiO_2 microbridge. The boron doping concentrations were from 1×10^{16} to $5 \times 10^{19} \text{ cm}^{-3}$. The dimensions of the SiO_2 microbridge were 400 μm in length, 50 μm in width, and 1 μm in thickness. The piezoresistors were 400 μm in length, 2 μm in width, and 2 μm in thickness.

3.4 Fabrication of SiO_2 microbridge with Si piezoresistors

We fabricated a microbridge with a commercially available SOI wafer (Figure 3.8). The dimensions of the designed microbridge were 400 μm in length, 50 μm in width, and 1 μm in thickness. The dimensions of the Si piezoresistor on the bridge were 400 μm in length, 10 μm in width, and 2 μm in thickness. The width of the piezoresistor was chosen to satisfy the resolution limitations of photolithography and to obtain a high

yield. From the simulation result, the microbridge sensor had the highest S/N ratio when the piezoresistor was from 1.2 μm to 2 μm thick. For SOI wafers available on the wafer market, the 2 μm thick device layer was the thinnest.

The designed fabrication process has four steps.

- First, pattern the piezoresistor on the top of the SOI wafer by photolithography and dry plasma etching.
- Second, pattern the bridge beam on the buried SiO_2 layer by a second photolithography process and buffered oxide etching (BOE).
- Third, pattern the electrode on the SiO_2 surface by using the metallization and lift-off method.
- Fourth, release the bridge from bulk Si by dry plasma etching.

The fabrication process of the piezoresistive Si on the SiO_2 microbridge is illustrated in Figure 3.8. PR 1813 was spun on the surface of SOI wafer. A piezoresistor pattern was transferred onto the photoresist layer on the front side of the wafer by a standard photolithography process and then the Si piezoresistor was formed by ICP etching. The photoresist was then removed by acetone and DI water (Figure 3.8(b)). A layer of PR 1813 was spun on the surface of the buried oxide layer of the SOI wafer. The microbridge beam pattern was transferred to the photoresist layer and then the SiO_2 beams were formed by etching with BOE. The photoresist was then removed by acetone and DI water (Figure 3.8(c)).

Next, the LOR 7B photoresist lift-off processing method was employed for electrode pad fabrication. Firstly, a layer of LOR 7B photoresist was spin-coated on the wafer, followed by a layer of PR 1813. The contact electrode pattern was positioned on

the bare area of the wafer. Because LOR B photoresist series have relatively high dissolution rates, an undercut profile was achieved and the lift-off was easily accomplished. A thin film of gold was deposited. Ultrasonic was used to remove the photoresist, leaving a gold pad on the SiO₂ (Figure 3.8(d)). Finally, a 20- μ m-thick photoresist AZ 9260 was spun on the backside of the wafer followed by a typical photolithography patterning process. The thick photoresist pattern served as a mask for deep Si plasma etching. The Si was etched off by using the ICP process to release the microbridge beams from the bulk Si (Figure 3.8(e)). During ICP etching, the wafer was inspected frequently to see whether the desired etching thickness was reached. Neither the piezoresistor nor the metallization would be damaged during the etching. The SEM picture of a fabricated microbridge is shown in Figure 3.9.

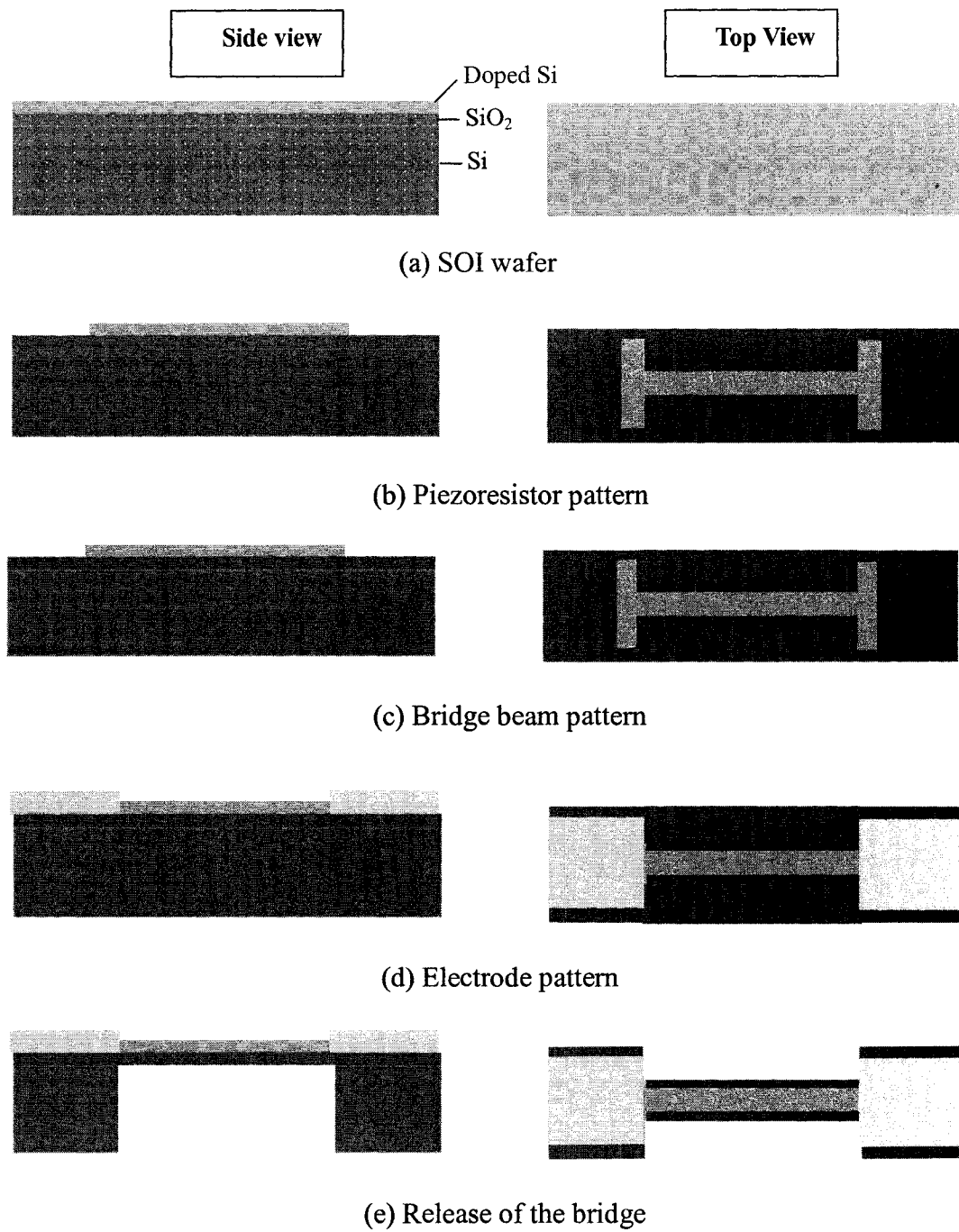


Figure 3.8 Fabrication process for SiO₂ supported piezoresistive microbridges.

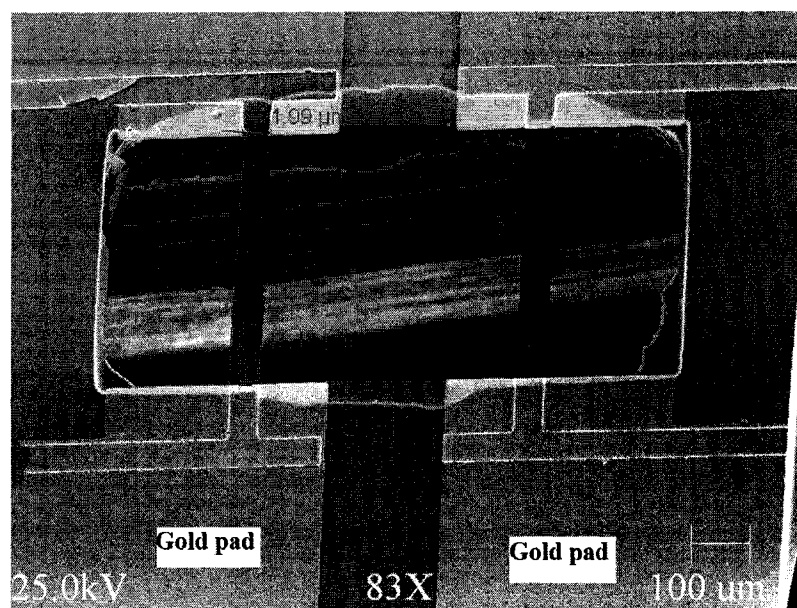


Figure 3.9 SEM picture of piezoresistive Si on an SiO₂ microbridge. The dimensions of the SiO₂ microbridge were 400 μm in length, 50 μm in width, and 1 μm in thickness. The piezoresistor was 400 μm in length, 10 μm in width, and 2 μm in thickness.

We investigated the detection of Hg²⁺ based on the microbridge platform for sensor validation. In our preliminary verification experiments, we coated a thin layer of polystyrene on the Si side of the microbridge to prevent the Si resistor and gold pads from exposure to testing solutions. The other side of the SiO₂ microbridge was coated by a thin layer of gold that will react with Hg²⁺ in the solution. We have reported that an equivalent of 2 N/m surface stress will be generated on a gold surface after a gold surface was exposed to a 10⁻⁶ M Hg²⁺ solution for 20 minutes [13].

A gold coated microbridge was initially exposed to a solution containing 1x10⁻⁶ M HNO₃ and the microbridge was equilibrated until a stable baseline was obtained. The resistance of the microbridge was measured using a Keithley Test Station (236 Source Measurement Unit). Figure 3.10 shows that, when the solution was replaced by a 1x 10⁻⁶ M solution of Hg²⁺ in 1x10⁻⁶ M HNO₃, the resistance of the piezoresistive microbridge

changed from 2.24534 M Ω to 2.24556 M Ω after 20 min, i.e. the $\Delta R/R$ change of the microbridge was 9.8×10^{-5} . This result matches very well with $\Delta R/R = 1.2 \times 10^{-4}$ obtained from the simulation results for a microbridge with the same dimensions as shown in Figure 3.3(a).

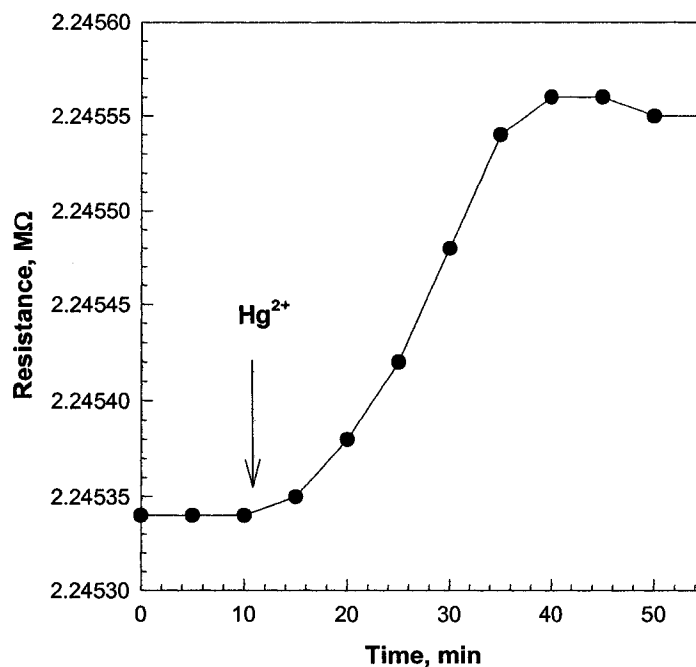


Figure 3.10 The resistance change of a piezoresistive Si on SiO₂ microbridge upon exposure to a 10^{-6} M of Hg²⁺. The dimensions of the SiO₂ microbridge were 400 μm in length, 50 μm in width, and 1 μm in thickness. The piezoresistor was 400 μm in length, 10 μm in width, and 2 μm in thickness.

3.5 Conclusion

Finite elements analysis was used to study the performance of Si covered SiO₂ microbridges for sensing applications. Various parameters, such as thickness, width, and doping concentration of the Si were investigated. The results showed that although the $\Delta R/R$ of the microbridge increases when the thickness decreases, the S/N ratio does not change significantly from 2 μm to 0.2 μm thickness. The piezoresistive microbridges

were fabricated and the results validated that these microbridges can be used for developing chemical and biological sensors.

CHAPTER FOUR

MICROCOILS FOR CHEM/BIO SENSING

4.1 Introduction

The first crude hygrometer was built in the 1400s by Leonardo da Vinci. Francesco Folli invented a more practical hygrometer in 1664. In early 1700, Robert Hooke invented the first balance spring or coil that improved the meteorological instruments, such as the barometer, anemometer, and hygrometer, etc [79]. In a dial hygrometer, a humidity sensitive polymer coated strip coil is attached to a dial to indicate humidity. The coils undergo extension or contraction due to moisture vapor absorption by confining the absorption to one side of the coil. When the relative humidity increases, the polymer swells which extends the coil and pulls the dial hand in one direction. At a low relative humidity, the polymer releases the tension on the coil, which allows the dial hand to move in the opposite direction.

Although the bilayer-based dial barometer, thermometer, and hygrometer have been used for several centuries, no other sensors have been developed based on this device. Recently, we realized that this bilayer-based dial hygrometer might be used as a universal tool for the detection of chemical species by depositing a chemical specific coating on one side of the coil. If appropriately designed, the concentration of chemicals can be directly read by the human eye by observing dial hand movement or be accurately measured in the

electrical domain by observing the change in the conductance or resistance of a piezoelectric material coated onto the coil. In this work, we report the proof-of-concept of a novel coil and microcoil based sensor platform.

4.2 Power-free Coil Sensors

The spring coil component can be made of any thin, elastic material, including polymers, composites, metals, alloys, etc. The size varies for different applications. We used a brass coil for power-free chemical measurement. The dimensions of this coil were 75 μm in thickness, 3 mm in width and 10 cm in length in the extended form.

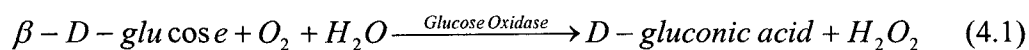
In a simple test for detection of chemical species in air, we coated polypyridine (PV), an alcohol sensitive polymer [80], on one side of a coil for alcohol detection. The dial hand of the PV coated coil moved to the right upon exposure to alcohol, indicating the swelling of the PV polymer. We named the device a dial alcoholmeter, an economic device for alcohol measurement.

Hydrogels were used to confirm the sensing ability of the coil in solutions. Polymers, such as stimuli-responsive hydrogels, change volume in response to small changes in ionic strength, pH, or specific analytes in solution [81], [82]. The reversible swelling property of hydrogels has also been used to develop chemical and biological sensors [83] - [85]. For chem/bio sensing, a molecular recognition agent that selectively interacts with specific molecules could be attached to the polymer chain. The sensor platforms include electrode [83], fluorescence [84], crystalline colloidal array reflection [85] etc. The swelling behaviors of hydrogels are ideal for developing coil-based chemical and biological sensors in solution. Since intelligent hydrogels swell in response to the concentration of particular analytes and the gel volume is a function of analyte

concentration, the swelling of the gel will extend or open the coil and cause the movement of the dial hand. This will occur only when the hydrogel is secured on one side of the coil strip.

A hydrogel that contains amino (or carboxyl) groups can be used for pH measurement. The minimum gel volume occurs at high pH where the NH_2 groups are saturated. At lower pH, the amino groups of the gel tend to be protonated, and the gel expands because of increased electrostatic repulsion between the cationic chains and the increase in the Donnan osmotic pressure [85]. We spread an acrylamide precursor solution on a brass strip, and exposed this strip to UV light to form a hydrogel on the strip. Then we formed the strip into a coil and attached a dial hand to the center of the coil. The resulting gel coated coil was equilibrated in a $\text{pH} = 7.0$ buffer solution for 1 day before testing in different buffer solutions at different pH values. All the phosphate buffer solutions had the same buffer concentration (0.01M) and ionic strength with different pH. When the pH was >7 , the coil dial hand turned left indicating that the gel had contracted. When the pH was <7 , the coil dial hand turned right indicating that the gel had swelled. For example, the dial hand turned right to 46° at $\text{pH} 5.8$, and left at -93° at $\text{pH} 8.1$. Since most intelligent gels are relatively homogeneous materials that shrink or swell uniformly with no dramatic change in shape, the coil expansion is reversible and reproducible.

Another example is to develop a Glucose Oxidase (GOx) containing hydrogel modified coil for the measurement of glucose. GOx is a highly specific enzyme that oxidizes [86], [87] glucose and produces gluconic acid and hydrogen peroxide.



The generation of gluconic acid is capable of promoting electroosmotic swelling of the gel due to the formation of charged ions, including gluconate and proton, and also for the subsequent swelling of the gel. As expected, when the coil was placed in a glucose concentration, the coil dial hand turned left indicating that the gel had contracted.

We expect to develop an array of coil based sensors, where each individual sensor will detect different chemicals or biomolecules and different concentration ranges. The dial hand movement will be read from the calibrated numeral dial face for different analytes in solution. This technology may provide a simple, power-free kit for environmental or clinical diagnostics.

4.3 Microcoil Sensors

The coil movement can be readily observed by the human eye and it presents a cost-effective and power-free device. However, due to the relative large size, the dynamic response time of this coil device can not compete with many other micro and nanosensors. It is expected that a coil device at micro- or nano-scale size will provide an outstanding sensor platform offering an improved dynamic response, greatly reduced size, and the integration of micromechanical components with on-chip electronic circuitry. In this work, we fabricated a $\text{SiO}_2/\text{Si}/\text{SU-8}$ trilayered microcoil for sensing validation. The piezoresistive property of the doped Si was used to determine the adsorption/absorption induced microcoil extension.

A fabricated trilayered microcoil/microspring is shown in Figure 4.1. The diameter of the microcoil was approximately 600 μm . In the extended form, the dimensions of the microcoil were 9.8 mm in length, 50 μm in width, and 28 μm in thickness.

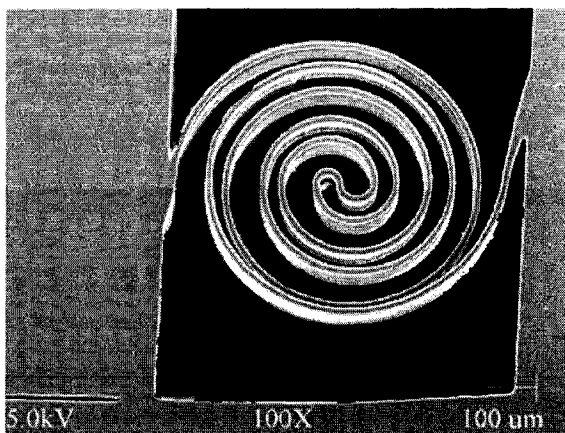


Figure 4.1 The SEM picture of a SiO₂/Si/SU-8 trilayered microcoil and array. In the extended form, the dimensions of the microcoil were 9.8 mm in length, 50 μm in width, and 28 μm in thickness. The coil size was 500 μm × 600 μm. The thickness of the Si and SU-8 layer were 8 and 20 μm, respectively. For fabrication simplicity, the coil was made in a structure that the two ends of the coil were attached to two pads outside of the coil. To match with this structure, the specially designed SU-8 layer was kept on the outside surfaces of the coil in order to achieve a uniform contraction or expansion of the coil, i.e. the SU-8 layer from the bottom pad to the center was not connected with the SU-8 from the top pad to the center.

4.4 Fabrication Process

A commercially available Si wafer was used to fabricate the microcoils. The fabrication process is illustrated in Figure 4.2.

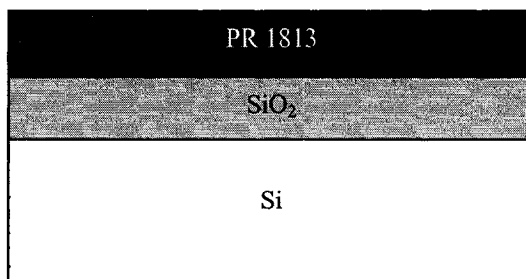
First, pattern the Si-layer coil by photolithography and BOE etching; PR 1813 was spun on the surface of the Si wafer (Figure 4.3(a)). The Si coil pattern was transferred to the photoresist layer on the front side of the wafer by a standard photolithography process (Figure 4.2(b)-(c)) and a SiO₂ mask was formed by BOE wet etching (Figure 4.2(d)). Then the patterned Si wafer was put into ICP system to form the Si coil (Figure 4.2(e)).

After removing the PR 1813 with acetone (Figure 4.2(f)) and then the SiO₂ mask with BOE etching (Figure 4.2(g)), the Si coils were then metalized (Figure 4.2(h)) which

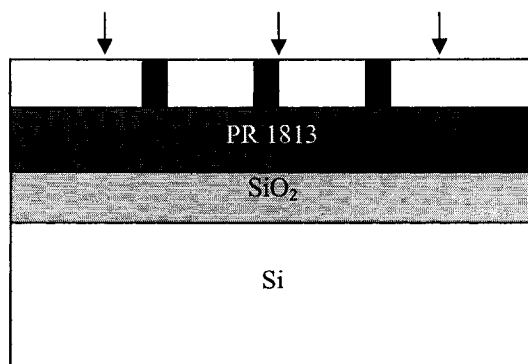
was realized by depositing platinum and then performing the lift-off patterning process. The metallization serves as the connecting interface for the Si coil to the outside circuit board by connecting both ends with a metal pad.

The next step was to put the wafer into the oxidation furnace to grow a 1 μm thick SiO_2 film on the sidewalls (Figure 4.2(i)). Depending on the temperature setting of the furnace, this process could take as long as 12 hrs. Then SU-8 negative photoresist was spin-coated on the front side of the wafer and photolithography was used again to form the polymer coil layer (Figure 4.2(j)-(l)).

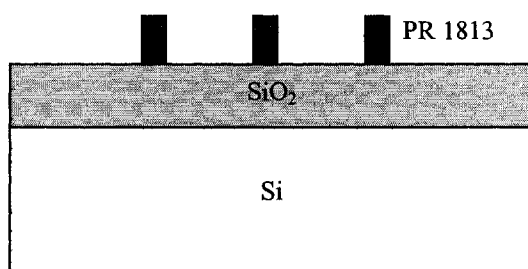
The last step of the fabrication procedure involved the backside ICP etching process to release the microcoil from the substrate. This was realized again by photolithography to define the etching pattern before ICP etching (Figure 4.2(m)). Figure 4.2(a)-(m) is shown below.



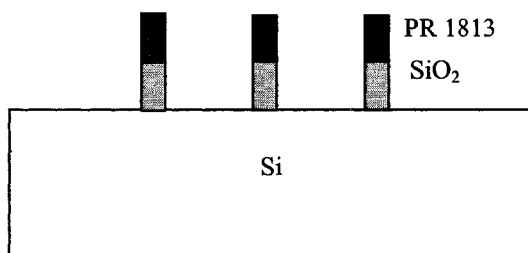
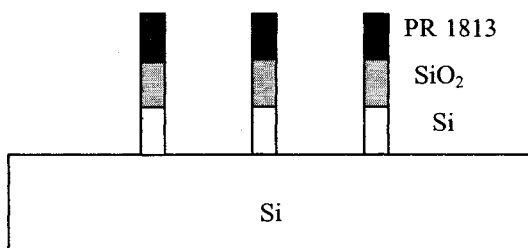
(a) Spin-coating of PR 1813 and Soft Bake



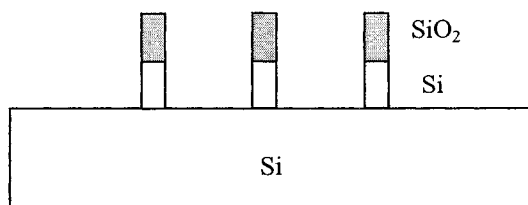
(b) Exposure to UV light



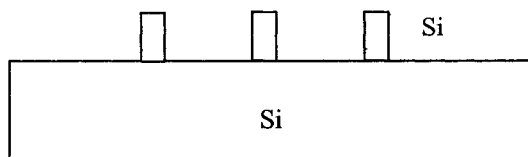
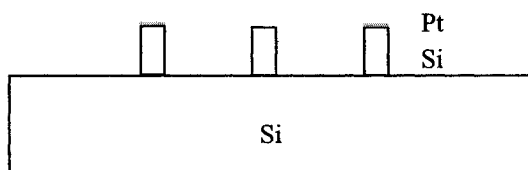
(c) Development of exposed S1813 and Hard Bake

(d) BOE etching to get SiO₂ mask for ICP etching

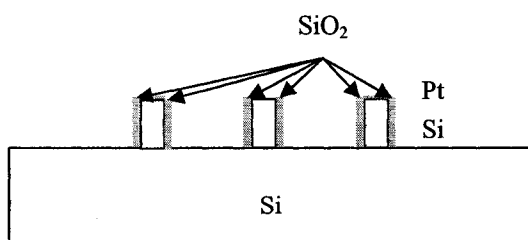
(e) ICP to get Si coil.



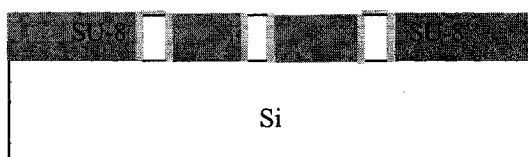
(f) Use Acetone to remove PR 1813

(g) BOE etching to remove SiO₂ and oxidation

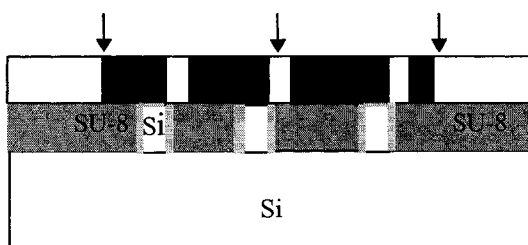
(h) Metallization realized by lift-off



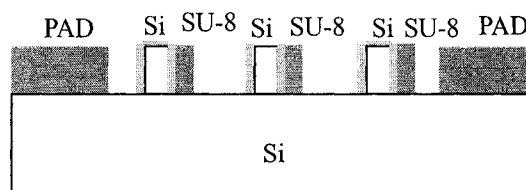
(i) Sidewall oxidation



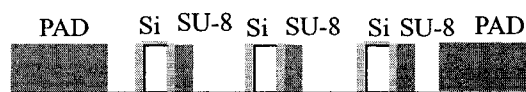
(j) Spin-coating SU-8 and Soft bake



(k) Exposure to UV light



(l) Development and Hard Bake



(m) ICP process of back side to release the coil

Figure 4.2 Fabrication process for the microcoils.

4.5 Results and Discussions

ICP etching is a chemical dry etching technique that offers many advantages over wet chemical etching methods, including high etch rate, compatibility with traditional IC processing [88] and high Si:SiO₂ etching selectivity (up to 350:1) [89]. The high selectivity is a great advantage in producing the Si coil as well as releasing the coil from bulk Si. Deep dry plasma etching achieves a high etching rate and straight sidewalls. In an ICP etching process, the flow rates of SF₆ and C₄F₈ and the SF₆/C₄F₈ ratio are the critical parameters for controlling the quality of the Si microcoils.

Factors that affect the rate and quality of plasma etching are gas flow, pressure and R.F. power. The gases used determine the efficiency and selectivity of the etching. This is the first parameter to choose when establishing an etching recipe. Equilibrium between the R.F. power and the gas flow controls the ionization rate of the gases, while a higher pressure increases the probability of ions impacting on the target material. The gas flow rate controls the rate at which products are evacuated from the chamber.

The etching rate was slow when the SF_6 and C_4F_8 flow rates were low. On the other hand, undercut occurred when a fast SF_6 flow rate and a large $\text{SF}_6/\text{C}_4\text{F}_8$ ratio were used. Figure 4.3 shows microcoils fabricated using an ICP recipe with 1800W power, 300 sccm SF_6 , 50 sccm C_4F_8 , 30W bias power and 18% pressure.



Figure 4.3 Microcoils fabricated using an ICP recipe with 1800W power, 300 sccm SF_6 , 50 sccm C_4F_8 , 30W bias power and 18% pressure.

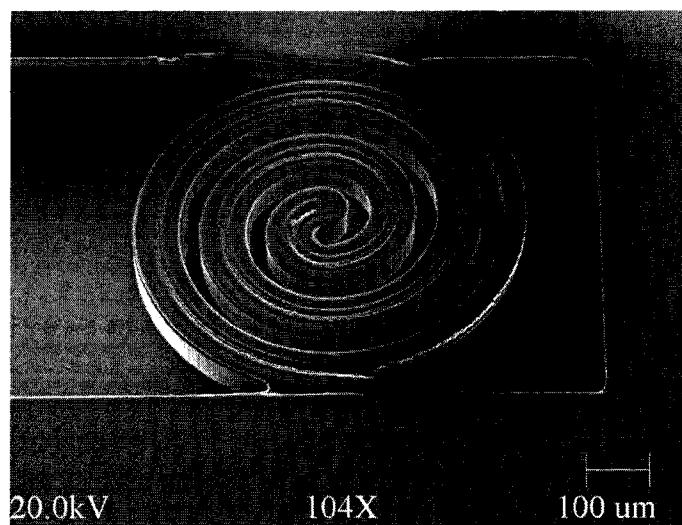
Since the width of the microcoil designed was only 10 μm , ICP recipes for small features would be needed. Through multiple test runs of the system, optimized parameters for controlling the etching can be obtained. One recipe that was successfully used in this work was 1800 W power, 300 sccm (standard cubic centimeters per minute) SF_6 , 150 sccm C_4F_8 , 50 W bias power and 20% pressure.

The processing of SU-8, an epoxy based negative photoresist, was another challenge to produce a thin SU-8 coated microcoil with high uniformity. SU-8 was selected in this work as the negative photoresist for microcoil patterning and then formed part of the structure. It has high functionality, high optical transparency and is sensitive to

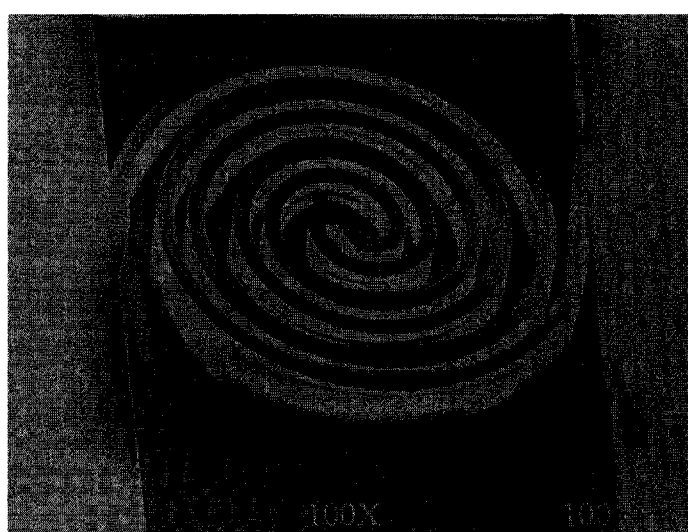
near UV radiation. Cured SU-8 is highly resistant to organic solvents, acids, and bases and has excellent thermal stability, making it well suited for applications in which cured polymer structures are a permanent part of the device [90], [91]. In this work, after photolithography, SU-8 was left on the wafer to act as one layer of the desired coil structure.

In these experiments, SU-8 50 was used and processed according to the standard process procedures discussed in Chapter 2. After baking, the wafer was exposed to near UV (350 nm) light for 50 seconds to cross-link the patterned area. This exposure time was well controlled. Over exposure (120 seconds in Figure 4.4(a)) would result in crosslinking of the photoresist adjacent to the exposed area. As a comparison, 50 seconds exposure time would provide the designed SU-8 thickness and shape (Figure 4.4(b)).

Post-exposure bake was performed for 1 min at 65 °C and 8 min at 95 °C to further cross-link the exposed portions of the film. In the next photoresist developing process, the wafer was put into SU-8 developer for 6 minutes. Strong agitation, such as ultrasonic, was used to improve the results of the developing process.



(a)



(b)

Figure 4.4 Microcoil developed after 120 seconds (a) and 50 seconds (b) exposure to the UV light.

4.6 Sensing Behavior of the Microcoils.

It was anticipated that microcoils could expand or contract upon the binding of a specific species in the environment and depending on the surface stress or energy applied on one surface of the microcoil, as shown in Figure 4.5.

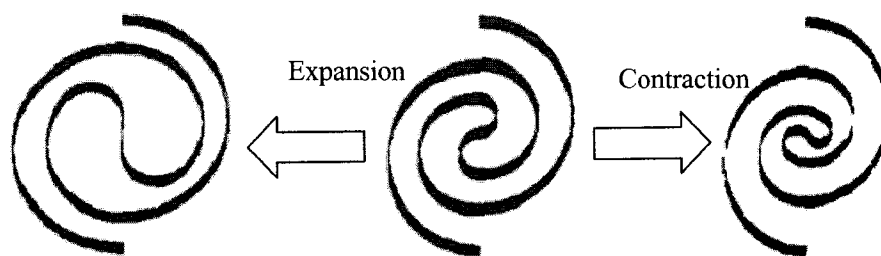


Figure 4.5 The coil movement when the inside surface is expanded (left) or contracted (right).

To demonstrate the concept of microcoil-based sensors, we modified the Si side of a microcoil with a thin film of amines by treating the coil with aminopropyltriethoxysilane (APS) according to a typical Si surface modification procedure [92].

Liquid phase APS treatment was carried out by immersing the microcoil into a solution of 2 mL of APS in 40 mL of toluene or xylene for 12 hours, followed by rinsing with DI water and blowing dry with nitrogen. Figure 4.6 schematically illustrates the aminopropylsilanation treatment process.

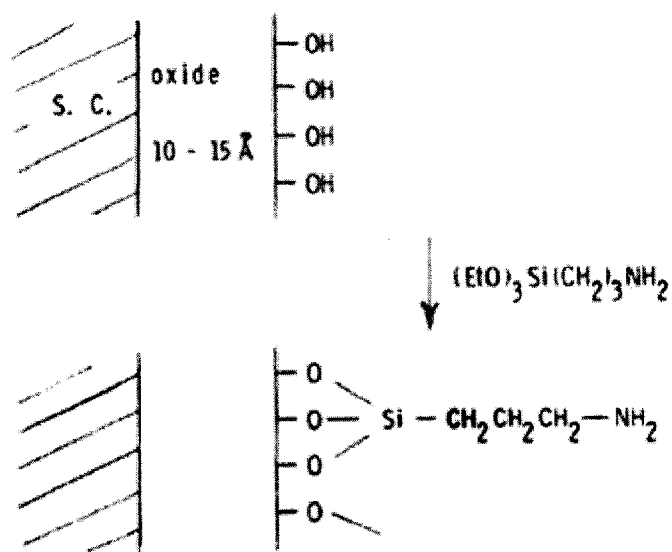
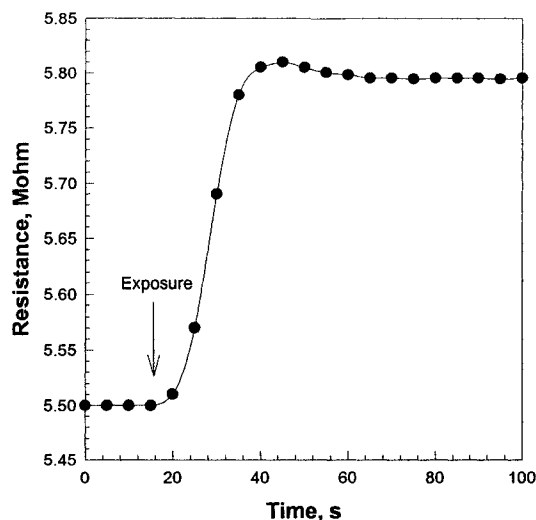


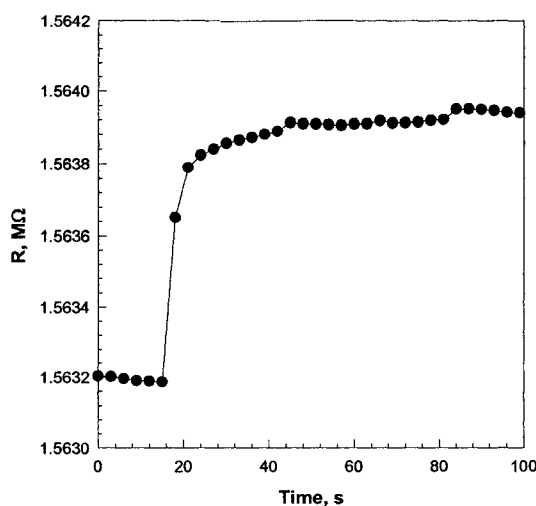
Figure 4.6 Monolayer reaction of APS on Si surface [92].

The resistance of the microcoil was measured by the Keithley Test Station (236 Source Measurement Unit). As expected, the resistance of the microcoil changed in an acidic environment, as shown in Figure 4.7(a). Our results showed that the resistance of the microcoil changed from $5.50 \pm 0.01 \text{ M}\Omega$ to $5.78 \pm 0.01 \text{ M}\Omega$ upon exposure to a 2.1% acetic acid vapor in air. It is known that when a piezoresistive material, such as doped Si, is under stress, its resistance changes. The results suggested that the interaction of acids with amino groups on the Si surface produced changes in free surface energy [93] that extended the coil and resulted in the sequent resistance change of the coil. A control experiment showed that a microcoil without amine film did not change its resistance upon exposure to acids, ruling out the possible interaction of acetic acid molecules with the Si surface or the SU-8 polymer. Another control experiment was performed on an aminopropyltriethoxysilane modified SiO_2/Si strip on a wafer. The dimension of this strip was the same as an extended microcoil, i.e. 7.7 mm in length, 50 μm in width. The results showed that the resistance change of the strip was negligible upon exposure to 2.1%

acetic acid. These experiments confirmed the resistance change was caused from surface stress induced microcoil expansion.



(a)



(b)

Figure 4.7 The resistance change of (a) an aminopropyltriethoxy-silane modified Si/SU-8 bilayered micro-spiral spring and (b) a piezoresistive microcantilever before and after exposure to 2.1% acetic acid in air. In the extended form, the dimensions of the microcoil were 7.7 mm in length, 50 μm in width, and 28 μm in thickness. The dimensions of the SiO₂ cantilever were 250 μm in length, 100 μm in width, and 1 μm in thickness. The Si piezoresistors on the SiO₂ cantilever was 100 μm in length, 20 μm in width, and 2 μm in thickness.

Recently, microcantilevers have proven to be an attractive platform for sensors with on-chip electronic circuitry and extreme sensitivity [94], [95]. The microcoil device functions similar to a microcantilever device. We compared the results from microcoils with those of microcantilevers. The $\Delta R/R$ change of this coil to the acetic acid vapor is 5.1%, which is significantly bigger than 0.03% of a Si cantilever sensor upon exposure to the same amount of acetic acid vapor. The noise over resistance ratio (noise/R) of the microcoil and microcantilever were 8.6×10^{-4} and 6.4×10^{-5} , respectively, as shown from Figure 4.7. The signal/noise (S/N) ratio at equilibrium of the microcoils and microcantilevers were 60 and 8, respectively, i.e. the S/N ratio of the microcoil was approximately 7.5 times of that of the microcantilever. These results suggest two advantages of the microcoil over the microcantilever sensor:

First, the $\Delta R/R$ of the microcoil is large enough to be measured by a simple circuit without amplifiers. This significantly lowers the cost of the device.

Second, the S/N ratio of the microcoil is larger than the microcantilever device, suggesting that the microcoils are more sensitive than the cantilevers. A lower detection limit for the microcoil device as compared to the microcantilever device is expected.

4.7 Conclusions

In conclusion, this work first reported that coils and microcoils can be widely used for detection of chemical and biological species both in air and in solutions. The fabrication process of $\text{SiO}_2/\text{Si}/\text{SU-8}$ trilayered microcoils has been discussed. This microcoil device has a potential to be used as a novel microsensor design for the detection of chemical and biological species both in air and in solutions.

In addition to the polymer and silane films studied in this work, many other approaches can also be used to immobilize the molecular recognition agent onto the coil surface, such as self-assembled monolayers on gold (SAM), surface conjugation chemistry and self-assembled monolayer, etc. Using the same coil/microcoil and even nanocoil device, numerous molecular or biomolecular recognition agents could be immobilized onto the coil surface for the detection of various chemical/biomolecular materials. The chemical selectivity may be achieved by a wide variety of antibody-antigen interactions, protein-protein interactions, DNA hybridizations and chemical recognition by a number of selective host molecules, such as crown ethers, calixarenes, cyclodextrins, and cryptand derivatives, etc.

CHAPTER FIVE

FABRICATION AND CHARACTERIZATION

OF GOLD AND PLATINUM NANOWIRES

5.1 Introduction

Metallic nanowires are one-dimensional, conductive nanostructures. They are expected to play an important role as interconnections and functional units in electronic and mechanical devices with nanoscale dimensions. In general, patterned metallic nanowires on surfaces are prepared using three approaches. The traditional lithography approach includes UV lithography, e-beam [96], [97], focused-ion-beam [98], proximal probe writing [99], [100], and DUV [101], [102] etc. The second approach takes advantages of existing nanostructures on surfaces or in solutions, such as porous alumina [103], [104] or micelles [105], [106], for template synthesis of metallic nanowires in solution and then aligned on surfaces. Self-assembly is the third approach, which has been generally explored as a bottom-up technique for generating complex nanostructures. Nanowires have been assembled from a colloidal system of metallic nanoparticles suspended in water [107] or from ionic solutions of the targeted metals [108].

In this paper, we report another direct, self-assembled approach to grow nanowires on a surface using an electrolysis process. Gold and Platinum nanowires have been produced between two microfabricated electrodes. Our long term goal is to investigate nanowire-based MOSFET sensors.

5.2 Experiments

In our design, two gold electrodes with a 150 nm thickness were fabricated using standard UV lithography and lift-off techniques. Electrodes with different gaps of 5 μm , 10 μm , 20 μm , 40 μm , and 120 μm were tested. Figure 5.1 shows the schematic diagram of the electrodes used in this work. The pads on each end of the electrodes were designed for wiring.

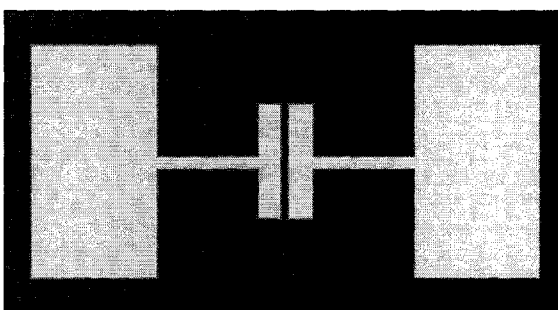
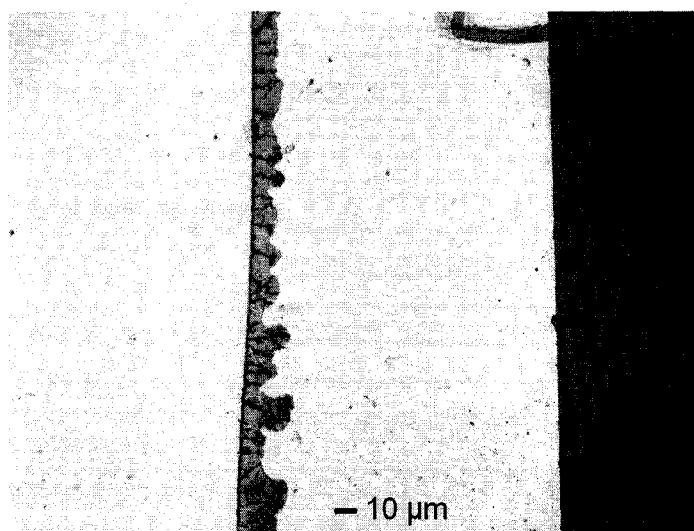


Figure 5.1 A schematic diagram of the gold electrodes. The electrodes were made on a Si wafer covered by 300-nm-thick SiO_2 .

In these experiments, the two electrodes were immersed into ethanol. By applying a sinusoidal signal to the electrodes and adjusting the amplitude and the frequency of the function generator, nanowires were generated between the two electrodes within two to three minutes (Figure 5.2). Typically, when the electrical signal was applied, the cathode remained intact while the anode was gradually oxidized and irregularly etched away from the cathode. This process was accompanying the formation of the nanowires. The nanowires were distributed along the cathode (Figure 5.2(a)) with 10 μm to 40 μm distance between two neighboring nanowires. The diameters of the nanowires were from 200 nm to 3 μm (Figure 5.2(a)-(b)). The growth of the nanowires was directed by the electric field and was perpendicular to the cathode edge. The gold nanowires formed into

dendrites near the irregular anode (Figure 5.2). The gold component of the nanowire was confirmed by energy dispersive spectrometry (EDS) analysis (Figure 5.3). It is noted that the Si and O were from the SiO_2 background (the teal colored areas, as shown in Figure 5.2(a)).



(a)



(b)

Figure 5.2 (a) Optical and (b) SEM images of the gold nanowires grown from an electrolysis process under an AC signal of 7 V_{rms} and 1 MHz with an DC offset of 10 V. The original gap between the two gold electrodes was 5 μm .

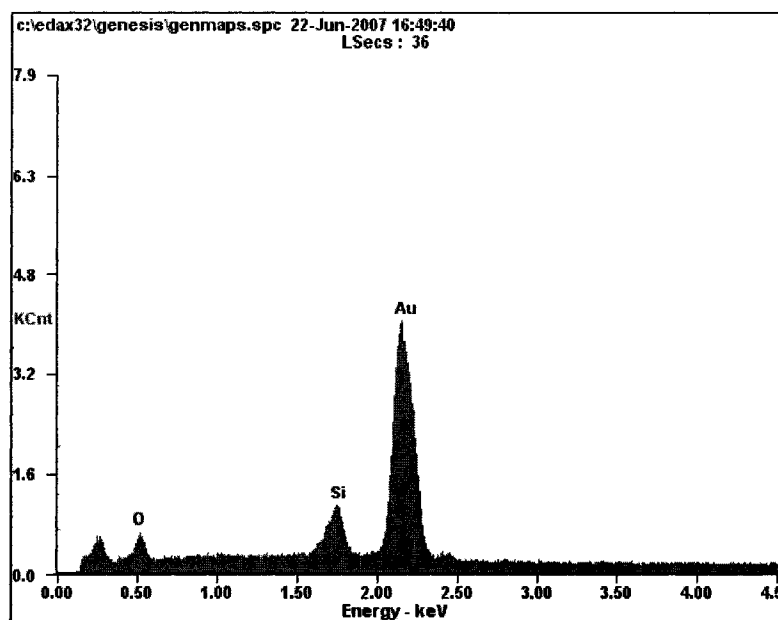


Figure 5.3 EDS analysis of the components of the gold nanowires and the adjacent SiO_2 surface.

5.3 Results and Discussions

The growth of the gold nanowires was affected by the amplitude of the applied DC offset, the frequency of the AC signal and the width of the gap between the two electrodes.

For a pair of electrodes with a 5 μm gap at low applied DC offset (< 2 V), no reaction occurred since the reduction potential of Au is 1.53 V. When the applied DC was from 2 V to 10 V, no nanowire was formed, but the anode was oxidized and gold particles were uniformly distributed on the cathode. This can be readily explained by an oxidation-reduction mechanism [109], i.e. the gold on the anode was firstly oxidized to Au^+ and/or Au^{3+} , and these ions were then reduced to gold particles on the cathode. At above 10 V DC offset, the nanowires appeared one minute after the bias was applied. Under this condition, the reduction of gold ions to particles was localized on the tip of

growing nanowire along the direction of the electric field [110] - [112]. This is reasonable since the electric field near the tip of the nanowire is the strongest and closest to the gold ions oxidized from the gold anode. These observations also demonstrated that a relatively strong electric field was needed to direct the growth of the nanowires.

For an electrode pair with a 5 μm gap, no nanowire growth was observed when only DC current or AC current was applied. Under DC, the gold particles were uniformly deposited onto the cathode to form a uniform film. The nanowires would grow only when both AC and DC were applied. The growth of the nanowires was only dependent on the DC voltage and not on the AC frequency.

Shorter gaps between the two electrodes facilitate the growth of the nanowires. Nanowires grew between 5 μm and 10 μm gaps in three minutes. No nanowire growth was observed between the two electrodes when the gap was 20 μm or greater.

It is expected that a similar result can be found from other metals. Figure 5.4 shows platinum nanowires produced under similar conditions. EDS analysis confirmed the platinum component of the nanowire (Figure 5.5). A minimum of 12 V DC offset is required for growing platinum nanowires. Instead of a relatively clean gold cathode surface as shown in Figure 5.2, platinum particles were widely observed on the platinum cathode during the oxidation-reduction process (Figure 5.4).

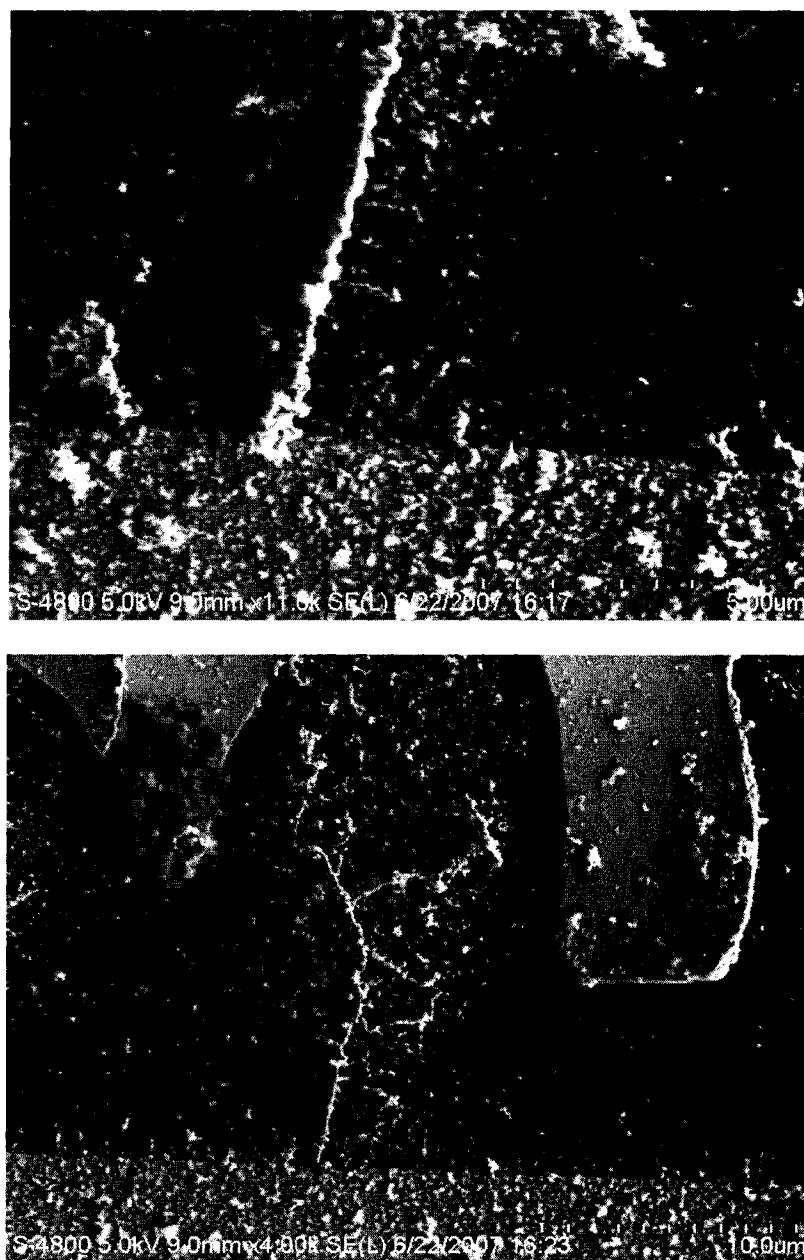


Figure 5.4 SEM images of the platinum nanowires grown from the electrolysis process under an AC signal of 9 Vrms and 10 Hz with an DC offset of 13 V.

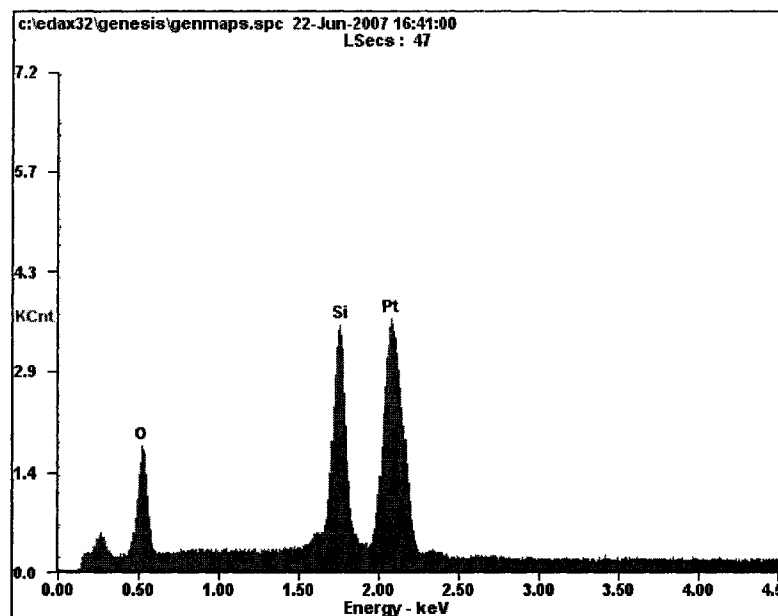


Figure 5.5 EDS component analysis of the Pt nanowires.

5.4 Conclusions

In summary, we demonstrated the formation of gold and platinum nanowires on surfaces during an electrolysis process. The practical application of the nanowires prepared under these conditions is unknown at this stage, however, the phenomena and formation mechanism might be used to grow nanowires directly from metal ions. We are currently investigating the feasibility and conditions to grow nanowires directly from the gold and platinum metal ions in solutions.

CHAPTER SIX

CONCLUSIONS AND FUTURE WORK

6. 1 Conclusions

In conclusion, novel microbridge chemical and biological sensors have been designed, simulated, fabricated and characterized in this work. Finite element analysis was used to study the performance of Si covered SiO₂ microbridges for sensing applications. Various parameters, including thickness, width and doping concentration of the Si, are important factors that determine the sensitivity of the microbridge sensor. It is seen from the simulation that the narrower, thinner and lower doping level the piezoresistor is, the higher sensitivity the microbridge exhibits. Although the $\Delta R/R$ of the microbridge increases when the thickness decreases, the S/N ratio decreases from 2 μm to 0.2 μm thickness. Based on the simulation result together with fabrication process availability, microbridges with the dimensions 400 μm in length, 50 μm in width, and 1 μm in thickness have been fabricated. The dimensions of the Si piezoresistor on the bridge were 400 μm in length, 10 μm in width, and 2 μm in width. The detection of the Hg²⁺ based on the microbridge platform was investigated for sensor validation. It was shown that the sensitivity of the fabricated microbridge is 0.0098%. The result matches well with the simulation results (0.012%) for a microbridge with the same dimensions. Compared with a microcantilever with the same dimensions, the sensitivity of the

microbridge is approximately 1/3 of that of the microcantilever, and the microbridge is approximately 50% more temperature dependent than the microcantilever.

SiO₂/Si/SU-8 microcoils have been fabricated following standard microfabrication technology. In the extended form, the dimensions of the microcoil are 9.8 mm in length, 50 μm in width, and 28 μm in thickness. The coil size is 500 μm × 600 μm. Liquid phase APS treatment was done according to a typical Si surface modification procedure. Verification of sensing has been done after surface modification. The ΔR/R change of this coil to the acetic acid vapor is significantly greater than that of a Si cantilever sensor upon exposure to the same amount of acetic acid vapor. The signal/noise (S/N) ratio at equilibrium of the microcoil and microcantilever were 60 and 8 respectively. The microcoil proves to be an attractive platform for sensors with on-chip electronic circuitry and extreme sensitivity.

Gold and Platinum nanowires with 200 nm to 3 μm diameter have been grown on an SiO₂ surface between two microfabricated electrodes using an electrolysis process under an AC signal with a DC offset. In this process, the anode electrode acted as a sacrificing layer and oxidized to metal ions. The metal ions were reduced to particles and aligned along the electric field to form nanowires connecting with the cathode. A minimum of AC signal of 10 V_{rms} and DC offset of 12 V were required for growing gold and platinum nanowires, respectively. Other factors affecting the growth of the nanowires include the frequency of the applied external bias and the width of the gap between the two electrodes. The potential of the nanowires to be used as chemical and biological sensors has yet to be investigated.

6. 2 Future Work

The microbridges and the microcoils are new chemical and biological sensors. Their corresponding mathematical models need to be constructed to further explore their physical characteristics. Also, new fabrication processes need to be investigated to improve the yield and reduce the production costs. Furthermore, new nanobridge and nanocoil devices could be designed to fabricate sensors with higher sensitivity. In addition to the polymer and silane films studied in this work, many other approaches can also be used to immobilize the molecular recognition agent onto the microbridge and coil surfaces, such as self-assembled monolayers on gold (SAM), surface conjugation chemistry and self-assembled monolayer, etc. Using the microbridge, microcoil and even nanobridge and nanocoil device, numerous molecular or biomolecular recognition agents could be immobilized onto their surfaces for various chemical/biomolecule detection.

The electrolysis approach to grow gold and platinum nanowires that was introduced in this work needs to be improved with respect to the nanowire growth condition in order to get more uniform and better aligned nanowires. The electrical properties of the nanowires should be characterized via proper instruments. Additionally, approaches to grow nanowires directly from gold and platinum metal ions in solution should be explored. The applicability of nanowires as a new kind of chemical and biological sensors needs to be effectively investigated.

REFERECES

- [1] H. Wohltjen, "Chemical microsensors and microinstrumentation," *Analytical Chemistry*, vol. 56, pp. 87A-103A, 1984.
- [2] M. Siegel, "Chemical Microsensors for Measurement Microsystems," *IEEE Instrumentation & Measurement Magazine*, vol. 7, pp. 27-32, 2004.
- [3] T. Thundat, R.J. Warmack, G. Y. Chen, and D. P. Allison, "Thermal and ambient-induced deflections of scanning force microscope cantilevers," *Applied Physics Letters*, vol. 64, pp. 2894-2903, 1994.
- [4] S. K. Vashist, "A Review of Microcantilevers for Sensing applications," *Journal of Nanotechnology Online*, vol. 3, pp. 1-15, 2007.
- [5] G.Y. Chen, T. Thundat, E. A. Wachter, and R. J. Warmack, "Adsorption-induced surface stress and its effects on resonance frequency of microcantilevers," *Journal of Applied Physics*, vol. 77, pp. 3618-3622, 1995.
- [6] Y. Tang, J. Fang, X. Yan, and H. Ji, "Fabrication and characterization of SiO₂ microcantilever for microsensor application," *Sensors and Actuators B*, vol. 97, pp. 109-113, 2004.
- [7] T. Thundat and P.I. Oden, "Microcantilever Sensors," *Microscale Thermophysical Engineering*, vol. 1, pp. 185-199, 1997.
- [8] W.Y. Shih, X.P. Li, and H.M. Gu, "Simultaneous liquid viscosity and density determination with piezoelectric unimorph cantilevers," *Journal of Applied Physics*, vol. 89, pp. 1497-1505, 2001.
- [9] E.S. Kolesar, P.B. Allen, and J.T. Howard, "Thermally actuated cantilever beam for achieving large in-plane mechanical deflections," *Thin Solid Films*, vol. 355-356, pp. 295-302, 1999.
- [10] K.-U. Kirstein, Y. Li, M. Zimmermann, C. Vancura, T. Volden, W. H. Song et al., "Cantilever-Based Biosensors in CMOS Technology," in *Proceedings of the Design, Automation and Test in Europe Conference and Exhibition*, vol. 2, pp. 1340-1341, 2005.

- [11] Y. Tang, J. Fang, X. Xu, H. Ji, G. M. Brown, and T. Thundat, "Detection of Femtomolar Concentrations of HF Using an SiO₂ Microcantilever," *Analytical Chemistry*, vol. 76, pp. 2478-2481, 2004.
- [12] T. Thundat, E. Finot, H. Ji, R. Dabestani, P.F. Britt, P.V. Bonnesen, G.M. Brown, and R.J. Warmack, "Highly selective microcantilever sensor for Cs ion detection," in *The Electrochemical Society Proceedings*, vol. 99-23, pp. 314-319, 1999.
- [13] H. Ji, T. Thundat, R. Dabestani, G.M. Brown, P.F. Britt, and P.V. Bonnesen, "Ultrasensitive detection of CrO₄²⁻ using a microcantilever sensor," *Analytical Chemistry*, vol. 73, pp. 1572-1576, 2001.
- [14] H. Ji and T. Thundat, "In situ detection of calcium ions with chemically modified microcantilevers," *Biosensors and Bioelectronics*, vol. 17, pp. 337-343, 2002.
- [15] X. Xu, T. Thundat, G. M. Brown, and H. F. Ji, "Ultrasensitive Detection of Hg²⁺ Using Microcantilever Sensors," *Analytical Chemistry*, vol. 74, pp. 3611-3615, 2002.
- [16] R. McKendry, J. Zhang, Y. Arntz, T. Strunz, M. Hegner, H.P. Lang, M.K. Baller, U. Certa, E. Meyer, H.J. Guntherodt, and C. Gerber, "Multiple label-free biodetection and quantitative DNA-binding assays on a nanomechanical cantilever array," in *Proceedings of the National Academy of Sciences*, vol. 99, pp. 9783-9788, 2002.
- [17] X. Yan, Y. Tang, H. Ji, Y. Lvov, and T. Thundat, "Detection of organophosphates using an acetyl cholinesterase (AChE) coated microcantilever," *Instrumentation Science & Technology*, vol. 32, pp. 175-183, 2004.
- [18] P. Decuzzi, A. Granaldi and G. Pascazio, "Dynamic response of microcantilever-based sensors in a fluidic chamber", *Journal of Applied Physics*, vol. 101, pp. 024303-024308, 2007.
- [19] D. Bornside, C. Macosko, and L. Scriven, "On the Modeling of Spin Coating," *Journal of Imaging Technology*, vol. 13, pp. 122-130, 1987.
- [20] L. Matthieu, "Discovering MEMS and microtechnology", Aug. 2007, http://matthieu.lagouge.free.fr/microtechnology/dry_etch.html.
- [21] S. Xu, K. N. Ostrikov, Y. Li, E. L. Tsakadze, and I. R. Jones, "Low-frequency, high-density, inductively coupled plasma sources: Operation and applications," *Physics of Plasmas*, vol. 8, pp. 2549-2557, 2001
- [22] M. Madou, *Fundamentals of Microfabrication*. New York: CRC Press, 1997.

- [23] X. Liu, "An intermediate-layer LITHOGRAPHY method for producing metal micro/nano patterns AND conducting polymer-based microdevices," Ph.D. Dissertation, Louisiana Tech University, Ruston, LA, 2007.
- [24] MEMS exchange, "MEMS Thin Film Deposition Processes", Aug. 2007, <http://www.memsnet.org/mems/processes/deposition.html>.
- [25] S. K. Ghandhi, 2nd Ed., *VLSI Fabrication Principles*. New York: John Wiley & Sons, 1994.
- [26] C. S. Smith, "Piezoresistance effect in germanium and silicon," *Physical Reviews*, vol. 94, pp. 42-49, 1954.
- [27] MicroChem, NanoTM SU-8 Negative Tone Photoresist Formulations 50-100, pp. 1-4
- [28] G. Binnig, C.F. Quate, and C. Gerber, "Atomic force microscope," *Physical Review Letters*, vol. 56, pp. 930-933, 1986.
- [29] E. M. A Rahman, M. I. Younis, and A. H. Nayfeh, "Characterization of the mechanical behavior of an electrically actuated microbeam," *Journal of Micromechanics and Microengineering*, vol. 12, pp. 759-766, 2002.
- [30] U. Bonne and D. Kubisiak, "Actuation based microsensors," *Smart Materials and Structures*, vol. 10, pp. 1185-1195, 2001.
- [31] Y. Ahn , G. Henry, and J. D. Zook, "Capacitive microbeam resonator design," *Journal of Micromechanics and Microengineering*, vol. 11, pp. 70-80, 2001.
- [32] M. W. Putty, "Process integration for active polysilicon resonant microstructures," *Sensors and Actuators A*, vol. 20, pp. 143-151, 1989.
- [33] J. D. Zook, "Characteristics of polysilicon resonant microbeams," *Sensors and Actuators A*, vol. 35, pp. 51-59, 1992.
- [34] Y. Ahn, "Resonant microbeam electronic oscillators for strain sensing," Ph.D. dissertation, University of Wisconsin-Madison, WI, 1999.
- [35] Y. Ahn and H. Guckel, "Fabrication process for high Q polysilicon beam resonators," *Sensors and Materials*, vol. 12, pp. 143-162, 1992.
- [36] J. J. Sniegowski, "Design and fabrication of the polysilicon resonating beam force transducers," Ph.D. dissertation, University of Wisconsin-Madison, WI, 1991.

- [37] H. Guckel, "Surface machined pressure transducers," *Sensors and Actuators A*, vol. 28, pp. 133-146, 1991.
- [38] S. Shin, S. Song, and Y. Lee, "Fabrication and electromechanical properties of piezoelectric micro-transducers for smart device," *Integrated Ferroelectrics*, vol. 54, pp. 679-687, 2003.
- [39] D. L. DeVoe, "Piezoelectric thin film beam resonators," *Sensors and Actuators A*, vol. 88, pp. 263-272, 2001.
- [40] M. Zanga, S. M. Zurn, D. L. Polla, B. J. Nelson, and W. P. Robbins, "Design, simulation and fabrication of a bridge structure microtransducer," in *International Conference on Modeling and Simulation of Microsystems*, pp. 265-268, 2000.
- [41] J. D. Zook, D. W. Burns, W. R. Herb, H. Guckel, J. W. Kang, and Y. Ahn, "Optically excited self resonant microbeams," *Sensors and Actuators A*, vol. 52, pp. 92-98, 1999.
- [42] J. W. Kang, "Design and fabrication of an amplitude detection polysilicon micromechanical resonating beam magnetometer," Ph.D. dissertation, University of Wisconsin-Madison, WI, 1996.
- [43] A. Voiculescu, M. Zaghoul, and R. A. McGill, "Design, fabrication and modeling of microbeam structures for gas sensor applications in CMOS technology," in *Proceedings of IEEE International Symposium on Circuit and Systems*, vol. 3, pp. III922-III925, 2003.
- [44] R. Legtenber, S. Bouswstra, and H. J. Jan, "Resonating microbridge mass flow sensor with low-temperature glass-bonded cap wafer," *Sensors and Actuators A*, vol. 27, pp. 723-727, 1991.
- [45] T. Matsuura, M. Taguchi, K. Kawata, and K. Tsutsumi, "Arcuation control of microbridge for flow sensor," *Sensors and Actuators A*, vol. 60, pp. 197-201, 1997.
- [46] D. Saya, L. Nicu, M. Guiradel, Y. Tauran, and C. Bergaud, "Mechanical effect of gold nanoparticles labeling used for biochemical sensor applications: A multimode analysis by means of SiN_x micromechanical cantilever and bridge mass detectors," *Review of Scientific Instruments*, vol. 75, pp. 3010-3015, 2004.
- [47] N. Chong, T. A. S. Srinivas, and H. Ahmed, "Performance of GaAs microbridge thermocouple infrared detectors," *Journal of Microelectromechanical System*, vol. 6, pp. 136-141, 1997.

- [48] J. Han, C. Zhu, J. Liu, and P. Li, "A novel temperature compensating structure for micromechanical bridge resonators," *Journal of Micromechanics and Microengineering*, vol. 15, pp. 702-705, 2005.
- [49] H. C. Mastrangelo, and R. S. Muller, "Microfabricated thermal absolute-pressure sensor with on-chip digital front-end processor," *IEEE Journal of solid-state circuits*, vol. 26, pp. 1998-2007, 1991.
- [50] R. J. Wilfinger, P. H. Bardell, and D. S. Chhabra, "The resonator: a frequency selective device utilizing the mechanical resonance of a silicon substrate," *IBM Journal of Research and Development*, vol. 12, pp. 113-118, 1968.
- [51] H. A. C Tilmans, M. Elwenspoekand, and J. H. J. Fluitman, "Micro resonant force gauges," *Sensors and Actuators A*, vol. 30, pp. 35-53, 1992.
- [52] A. N. Cleland and M. L. Roukes, "A nanometer scale mechanical electrometer," *Nature*, vol. 320, pp. 160, 1998.
- [53] C. Nguyen and R. Howe, "Electrostatic-comb drive of lateral polysilicon resonators," in *Proceedings of the IEEE International Frequency Control Symposium*, vol. 48, pp. 127, 1994.
- [54] B. H. Kim, D. P. Kern, S. Raible, and U. Weimer, "Fabrication of micromechanical mass-sensitive resonators with increased mass resolution using SOI substrate," *Microelectronic Engineering*, vol. 61-62, pp. 947-953, 2002.
- [55] K. L. Ekinci, X. M. H. Huang, and M. L. Roukes, "Ultrasensitive nanomechanical mass detection," *Applied Physics Letters*, vol. 84, pp. 4469-4471, 2004.
- [56] Y. T. Yang, K. L. Ekinci, X. M. H. Huang, L. M. Schiavone, M. L. Roukes, C. A. Zorman, and M. Mehregany, "Monocrystalline silicon carbide nanomechanical systems," *Applied Physics Letters*, vol. 78, pp. 162-164, 2001.
- [57] K. Yasumura, T. Stowe, E. Chow, T. Pfafman, T. Kenny, B. Stripe, and D. Rugar, "Quality factors in micron- and submicron- thick cantilevers," *Journal of Microelectromechanical Systems*, vol. 9, pp. 117-125, 2000.
- [58] H. B. Weber and R. Haussler, "Nonequilibrium electrostatic transport and interaction in short metallic nanobridges," *Physical Review B*, vol. 63, pp. 165426-1-6, 2001.
- [59] S. K. S. Ralls and R. A. Buhrman, "Microscopic study of 1/f noise in metal nano bridges," *Physical Review B*, vol. 44, pp. 5800-5817, 1991.

- [60] K. Prashant, L. Li, P. Boudreaux, and D. L. Devoe, "Fabrication of piezoelectric $\text{Al}_{0.3}\text{Ga}_{0.7}\text{As}$ heterostructures," *Journal of Microelectromechanical Systems*, vol. 5, pp. 51-55, 2003.
- [61] P. Bruschi, A. Nannini, and B. Neri, "Vapour and gas sensing by noise measurement on polymeric balanced bridge microstructures," *Sensors and Actuators B*, vol. 24-25, pp. 429-432, 1995.
- [62] M. Cole, J. W. Gradner, A. W. Y. Lim, P. K. Scivier, and J. E. Brignell, "Polymeric resistive bridge gas sensor array driven by standard cell CMOS current drive chip," *Sensors and Actuators B*, vol. 58, pp. 518-525, 1999.
- [63] C. Moldovan, B-H. Kim, S. Raible, and V. Moager, "Simulation and microfabrication of polysilicon structures used as mass sensitive sensors for gas detection," in *Proceeding of the International Semiconductor Conference*, vol. 2, pp. 459-462, 2000.
- [64] D. Moser, M. Parameswaran, and H. Baltes, "Field oxide microbridges, cantilever beams, coils and suspended membranes in SACMOS technology," *Sensors and Actuators A*, vol. 23, pp. 1019-1022, 1990.
- [65] M. Parameswaran, L. J. Ristic, A. C. Dhaded, and H. P. Baltes, "Fabrication of microbridges in standard complementary metal oxide semiconductor technology," *Canadian Journal of Physics*, vol. 67, pp. 184-189, 1989.
- [66] H. Huang, C. A. Zorman, M. Mehregany, and M. L. Roukes, "Nanodevice motion at microwave frequencies," *Nature*, vol. 421, p. 496, 2003.
- [67] R. T. Howe and R. S. Muller, "Frequency response of polycrystalline silicon Microbridges," in *IEEE International Conference on Solid-State Sensors and Actuators*, pp. 101-104, 1985.
- [68] T. Y. Zhang, Y. J. Su, C. F. Qian, M. H. Zhao, and L. Q. Chen, "Microbridge testing of thin films under small arcuation," in *Material Research Society Symposium Proceedings*, vol. 594, pp. 477-482, 2000.
- [69] A.C. Hiller and A.J. Bard, "Ac-mode Atomic Force Microscope imaging in air and solutions with a thermally driven bimetallic cantilever probe," *Review of Scientific Instruments*, vol. 68, pp. 2082-2090, 1997.
- [70] B. Firtat, C. Modovan, and D. Dascalu, "Microbridge Simulation for piezoresistive gas sensor detection," in *Proceedings of IEEE Semiconductor Conference*, pp. 63-66, 2002.

- [71] G. Vasile, C. Lepadatu, C. Moldovan, and O. Nedelcu, "Simulation and design of a resonant polysilicon Microbridge," in *Proceedings of IEEE Semiconductor Conference*, vol. 2, pp. 573-576, 2001.
- [72] R. B. Herring and L. P. Hunt, *Handbook of Semiconductor Silicon Technology*. New Jersey: William Andrew Publishing, 1990, p. 423.
- [73] M. Tortonese, R.C. Barrett, and C. F. Quate, "Atomic Resolution with an Atomic Force Microscope Using Piezoresistive Detection," *Applied Physics Letters*, vol. 62, pp. 834-636, 1993.
- [74] J. A. Harley and T. W. Kenny, "1/F Noise Considerations for the Design and Process Optimization of Piezoresistive Cantilevers," *Journal of Microelectromechanical Systems*, vol. 9, pp. 226-235, 2000.
- [75] M. T. Hou and R. Chen, "Effect of width on the stress-induced bending of micromachined bilayer cantilevers," *Journal of Micromechanics and Microengineering*, vol. 13, pp. 141-148, 2003.
- [76] S. D. Senturia, *Microsystems design*. Norwell: Kluwer Academic Publishers, 2000.
- [77] Y. Kanda, "A graphical representation of the piezoresistance coefficients in silicon," *IEEE Transactions on Electron Devices*, vol. 29, pp. 64-70, 1982.
- [78] J. C. Suhling and R.C.Jaeger, "Silicon piezoresistive stress sensors and their application in electronic packaging," *IEEE Sensors*, vol. 1, pp. 14-30, 2001.
- [79] E. A. Avallone and T. Baumeister, 11th Ed., *Marks's Standard Handbook for Mechanical Engineers*. New York: McGraw-Hill, 1997.
- [80] H. P. Lang, R. Berger, F. Battiston, J.P. Ramseyer, E. Meyer, C. Andreoli et al, "A chemical sensor based on a micromechanical cantilever array for the identification of gases and vapors," *Applied Physics A*, vol. 66, pp. 61-64, 1998.
- [81] A. R. Khokhlov and E. Yu, Kramarenko, "Weakly charged polyelectrolytes: collapse induced by extra ionization," *Macromolecules*, vol. 29, pp. 681-685, 1996.
- [82] T. Tanaka, "Collapse of gels and the critical endpoint," *Physical Review Letters*, vol. 40, pp. 820-823, 1978.
- [83] S. Herber, W. Olthuis, and P. Bergveld, "Exploitation of a pH-sensitive hydrogel disk for CO₂ detection ," *Sensors and Actuators B*, vol. 91, pp. 284-289, 2003.

- [84] R. Bashir, J. Z. Hilt, O. Elibol, A. Gupta, and N. A. Peppas, "Micromechanical cantilever as an ultrasensitive pH microsensor," *Applied Physics Letters*, vol. 81, pp. 3091-3093, 2002.
- [85] J. H. Holtz and S.A. Asher, "Polymerized colloidal crystal hydrogel films as intelligent chemical sensing materials," *Nature*, vol. 389, pp. 829-832, 1997.
- [86] S. J. Updike and G. P. Hicks, "The enzyme electrode," *Nature*, vol. 214, pp. 986-988, 1967.
- [87] L. C. Clark and C. Lyons, "Electrode systems for continuous monitoring in cardiovascular surgery," *Annals of the New York Academy of Science*, vol. 102, pp. 29-45, 1962.
- [88] T. Wang, C-H Chen, Y-S Lin, and S-S Lu, 2006, "A micromachined CMOS distributed amplifier by CMOS compatible ICP deep-trench technology," *IEEE Electron Device Letters*, vol. 27, pp. 291-293, 2006.
- [89] R. Feng and R. J. Farris, "Influence of processing conditions on the thermal and mechanical properties of SU8 negative photoresist coatings," *Journal of Micromechanics and Microengineering*, vol. 13, pp. 80-88, 2003.
- [90] J. M. Shaw, J. D. Gelorme, N. C. LaBianca, W. E. Conley, and S. J. Holmes, "Negative photoresists for optical lithography," *IBM Journal of Research and Development*, vol. 41, pp. 81-94, 1997.
- [91] V. Seidemann, J. Rabe, M. Feldmann, and S. Büttgenbach, "SU8-micromechanical structures with in situ fabricated movable parts," *Microsystem Technologies*, vol. 8, pp. 348-350, 2002.
- [92] I. Haller, "Covalently attached organic monolayers on semiconductor surfaces," *Journal of the American Chemical Society*, vol. 100, pp. 8050-8055, 1978.
- [93] R. Berger, E. Delamarche, H. P. Lang, C. Gerber, J. K. Gimzewski, E. Meyer, and H. Guntherodt, "Surface Stress in the Self-Assembly of Alkanethiols on Gold," *Science*, vol. 276, pp. 2021-2024, 1997.
- [94] H. P. Lang, M. K. Baller, R. Berger, C. Gerber, J. K. Gimzewski, F. M. Battiston, P. Fornaro, J. P. Ramseyer, E. Meyer, and H. J. Guntherodt, "An artificial nose based on a micromechanical cantilever array," *Analytica Chimica Acta*, vol. 393, pp. 59-65, 1999.

- [95] T. Thundat, E. A. Wachter, S. L. Sharp, and R. J. Warmack, "Detection of mercury Vapor using resonating cantilevers," *Applied Physics Letters*, vol. 66, pp. 1695-1697, 1995.
- [96] F. Cerrina and C. Marrian, "Patterned aluminum nanowires produced by electron beam at the surfaces of AlF_3 single crystals," *Solid State Communications*, vol. 129, pp. 681-685, 2004.
- [97] J. M. Gibson, "Reading and writing with electron beams," *Physics Today*, vol. 50, pp. 56-61, 1997.
- [98] S. Matsui and Y. Ochiai, "Focused ion beam applications to solid state devices," *Nanotechnology*, vol. 7, pp. 247-258, 1996.
- [99] S. H. Hong, J. Zhu, and C. A. Mirkin, "Multiple ink nanolithography: toward a multiple-pen nano-plotter," *Science*, vol. 286, pp. 523-525, 1999.
- [100] J. A. Dagata, "Device fabrication by scanned probe oxidation," *Science*, vol. 270, pp. 1625-1626, 1995.
- [101] M. D. Levenson, "Welcome to the DUV revolution," *Solid State Technology*, vol. 38, pp. 81-98, 1995.
- [102] S. Goolaup, A. O. Adeyeye, and N. Singh, "Magnetoresistance of closely packed $\text{Ni}_{80}\text{Fe}_{20}$ nanowires," *Thin Solid Films*, vol. 505, pp. 29-34, 2006.
- [103] Z. Liu and P. C. Searson, "Single nanoporous gold nanowire sensors," *Journal of Chemical Physics B*, vol. 110, pp. 4318-4322, 2006.
- [104] B. Nikoobakht, Z. L. Wang, and M. A. El-Sayed, "Self-assembly of gold nanorods," *Journal of Physical Chemistry B*, vol. 104, pp. 8635-8640, 2000.
- [105] C. J. Murphy, A. M. Gole, S. E. Hunyadi, and C. J. Orendorff, "One-dimensional colloidal gold and silver nanostructures," *Inorganic Chemistry*, vol. 45, pp. 7544-7554, 2006.
- [106] Y. Y. Yu, S. S. Chang, C. H. L. Lee, and C. R. H. Wang, "Gold nanorods: electrochemical synthesis and optical properties," *Journal of Physical Chemistry B*, vol. 101, pp. 6661-6665, 1997.
- [107] K. D. Hermanson, S. O. Lumsdon, J. P. Williams, E. W. Kaler, and O. D. Velev, "Dielectrophoretic assembly of electrically functional microwires from nanoparticle suspensions," *Science*, vol. 294, pp. 1082-1086, 2001.

- [108] C. Cheng, R. K. Gonela, Q. Gu, and D. T. Haynie, "Self-assembly of metallic nanowires from aqueous solution," *Nano Letters*, vol. 5, pp. 175-178, 2004.
- [109] J. Rodriguez-Fernandez, J. Perez-Juste, P. Mulaney, and L. M. Liz-Marzan, "Spatially-Directed Oxidation of Gold Nanoparticles by Au(III)-CTAB Complexes," *Journal of Physical Chemistry B*, vol. 109, pp. 14257-14261, 2005.
- [110] Y. J. Yuan, M. K. Andrews and B. K. Marlow, "Chaining and dendrite of formation of gold particles," *Applied Physics Letters*, vol. 85, pp. 130-132, 2004.
- [111] K. H. Bhatt and O. D. Velev, "Control and modeling of the dielectrophoretic assembly of on-chip nanoparticle wires," *Langmuir*, vol. 20, pp. 467-476, 2004.
- [112] A. Ramos, H. Morgan, N. G. Green, and A. J. Castellanos, "AC electric-field-induced fluid flow in microelectrodes," *Journal of Physics D*, vol. 31, pp. 2338-2353, 1998.